Journal of Applied Physics

Fluid and hybrid simulations of the ionization instabilities in Hall thruster

Cite as: J. Appl. Phys. **132**, 053301 (2022); https://doi.org/10.1063/5.0094269
Submitted: 01 April 2022 • Accepted: 03 July 2022 • Published Online: 03 August 2022

O. Chapurin, A. I. Smolyakov, G. Hagelaar, et al.

Journal of Applied Physics ARTICLE scitation.org/journal/jap

Fluid and hybrid simulations of the ionization instabilities in Hall thruster

Cite as: J. Appl. Phys. **132**, 053301 (2022); doi: 10.1063/5.0094269
Submitted: 1 April 2022 · Accepted: 3 July 2022 ·
Published Online: 3 August 2022

O. Chapurin,[1,a)] A. I. Smolyakov,[1] G. Hagelaar,[2] J.-P. Boeuf,[2] and Y. Raitses[3]

AFFILIATIONS

[1]Department of Physics and Engineering Physics, University of Saskatchewan, Saskatoon, Saskatchewan S7N 5E2, Canada
[2]LAPLACE, Université de Toulouse, CNRS, INPT, UPS, 118 Route de Narbonne, 31062 Toulouse, France
[3]Princeton Plasma Physics Laboratory, Princeton, New Jersey 08540, USA

[a)]**Author to whom correspondence should be addressed:** alex.chapurin@usask.ca

ABSTRACT

Low-frequency axial oscillations in the range of 5–50 kHz stand out as a pervasive feature observed in many types of Hall thrusters. While it is widely recognized that the ionization effects play the central role in this mode, as manifested via the large-scale oscillations of neutral and plasma density, the exact mechanism(s) of the instabilities remain unclear. To gain further insight into the physics of the breathing mode and evaluate the role of kinetic effects, a one-dimensional time-dependent full nonlinear low-frequency model describing neutral atoms, ions, and electrons is developed in full fluid formulation and compared to the hybrid model in which the ions and neutrals are kinetic. Both models are quasi-neutral and share the same electron fluid equations that include the electron diffusion, mobility across the magnetic field, and the electron energy evolution. The ionization models are also similar in both approaches. The predictions of fluid and hybrid simulations are compared for different test cases. Two main regimes are identified in both models: one with pure low-frequency behavior and the other one, where the low-frequency oscillations coexist with high-frequency oscillations in the range of 100–200 kHz, with the characteristic time scale of the ion channel fly-by time, 100–200 kHz. The other test case demonstrates the effect of a finite temperature of injected neutral atoms, which has a substantial suppression effect on the oscillation amplitude.

I. INTRODUCTION

Hall thrusters are successfully used for electric propulsion in space, e.g., for satellite orbit keeping, and becoming an enabling technology of choice for long-term missions, such as trips to Mars. Despite the relatively long history of practical use (since 1972[1]), the crucial physical aspects of their operation are poorly understood. In the absence of predictive modeling capabilities, scaling of these devices for large (e.g., for long-term missions) and for low (for microsatellites) power is very difficult and expensive. The quantitative understanding of the physics of these devices remains an important task.

The plasma discharge in Hall thrusters is supported by the electrons drifting in the closed azimuthal $E \times B$ direction. At the same time, ions create the thrust accelerated by the electric field in the axial direction; ions are effectively unmagnetized due to a large gyroradius. One of the characteristics of Hall thrusters is the presence of turbulence and structures (azimuthal and axial) that affect their operation. Studies of nonlinear phenomena in these plasmas are of great practical importance and address fundamental problems of plasma physics and plasma turbulence. In particular, the turbulent electron transport in such devices is orders of magnitude larger than the classical collisional transport across the magnetic field predicts. Inhomogeneous plasmas with $E \times B$ electron drift are typically prone to various drift instabilities, both due to the fluid[2] and kinetic mechanisms,[3–7] which drive high cross-field electron currents; more details can be found in Ref. 8.

Among the plethora of wave phenomena in a Hall thruster device, low-frequency oscillations propagating in the axial direction stand as one of the most common and observed in most types of Hall thrusters.[1] They appear as the axial discharge current oscillations with frequencies of 5–50 kHz.[9] A strong periodic depletion of atoms in the ionization region is observed during the oscillations, suggesting the ionization nature. In the literature, they are known as breathing modes due to slow periodic plasma bursts out of the channel exhaust. Analytical studies of these phenomena are difficult due to the importance of nonlinear effects and the global

nature of solutions; thus, numerical methods have to be used. Qualitatively, the oscillation period of breathing modes depends on the travel time of neutral particles to the ionization region, e.g., for its extent 1 cm and atom velocity 150 m/s gives 15 kHz. Overall, we understand the phenomenology of the oscillations but cannot accurately predict their existence and amplitude. A generally accepted phenomenological description of these oscillations is described as the following sequence: decrease of the discharge current → decrease of ionization → increase of the neutral density in the exhaust region → increase of the electron conductivity in that region → increase of the current and ionization → neutral depletion → decrease of the current, and so on. According to this picture, the oscillation frequency is related to the time necessary for the neutrals to refill the ionization region.

The 0D predator–prey model proposed earlier[10–12] is appealing because of its simplicity but fails to identify the conditions for the instability. Moreover, more accurate treatments show that the basic two-component (plasma-neutral) system with uniform ion and neutral velocities is stable.[12–14] A simple model was proposed that the ion backflow region, which occurs near the anode as a result of a large contribution of the electron diffusion current (due to the density gradient) and quasineutrality constraint, provides a critical excitation mechanism for the breathing mode.[13] Linear resistively unstable modes[15] and fluctuations of electron temperature and power absorption[12,14] were also investigated as possible triggers of the breathing modes. Reference 16 provides a general overview of physical mechanisms and stabilizing methods for breathing modes.

In general, several physical mechanisms affect the breathing mode excitation and characteristics: electron momentum and energy losses to the wall, anomalous cross-field transport and heating, the ion backflow, and recombination at the anode. These mechanisms are interrelated, depend in a complex way on the magnetic field configuration, and are not easily quantifiable. Numerical models that include many of these effects were proposed.[11,17–21] However, some calibration and adjustment of the parameters are required to satisfactorily reproduce the breathing mode characteristics observed experimentally.[22] Therefore, further insights on key physical processes are required to expand the predicting powers of such models, especially to the new parameter range and new operational regimes. Additionally, the external circuit effects can play an important role in low-frequency plasma oscillations.[14,23] One can propose active control algorithms for the discharge current stabilization by varying the external circuit components.[24] Self-stabilization of the low-frequency discharge current was observed when the electromagnet current is coupled to the discharge current.[25] In this paper, we do not consider these effects, focusing on the plasma dynamics, not including the external circuit.

While many time-dependent numerical models for breathing modes are based on fully fluid formulations, the hybrid modeling was also undertaken using the kinetic description for ions and neutrals.[15,19,20,26–28] The extent to which the ion and neutral kinetic effects influence the breathing mode excitation and characteristics remains a mute point of many studies. One of the goals of this paper is the analysis of the role of ions and neutral kinetic effects under the same physics of the electron dynamics, which is treated with the fluid theory. We use the axial one-dimensional full fluid and hybrid models and compare their results.

The basic fluid model describes ions and atoms with the two fluid moments, conservation of mass and momentum, and electrons are considered in a drift-diffusion approximation with a full electron energy balance. In the hybrid model, ions and atoms are kinetic via a particle-in-cell method, and electrons are fluid, modeled in the same way in both approaches. Both models include plasma recombination at the anode and neutral dynamics with ionization due to electron-neutral impact. The plasma discharge is supported by the ionization process driven by the axial current due to the applied potential across the domain. For the fluid simulations, a BOUT++ computational framework[29] is used. The hybrid code was developed in the LAPLACE laboratory, France.[18,30,31] This work is based on one of the test cases in the LANDMARK (Low temperAture magNetizeD plasMA benchmaRKs) project[32] and follows the setup initially proposed in LANDMARK.

Previously, a comparison between fluid and hybrid models for the axial direction of Hall thruster configuration was presented in Ref. 20. However, this model did not include electron pressure gradients, thus omitting the effects of electron diffusion, resulting in the formation of the presheath region near the anode and ion transition through the ion-sound barrier. Nor did it include the full electron energy balance.

One of the important findings of the present paper is the identification of two distinct regimes of breathing oscillations, the result of which was confirmed with both fluid and hybrid models during this benchmark. We show that the regime with higher electron energy losses exhibits the low-frequency mode of ≈14 kHz that coexists with the high-frequency ion "transient-time" oscillations of ≈150 kHz.[9] In the second regime, with low electron energy losses, pure breathing oscillations are observed, the so-called solo regime. We believe that different mechanisms are involved in these regimes.

For the first regime, we identify the high-frequency oscillations as the excitation of the resistive modes (convective instability with the characteristic ion fly-by frequency).[15,33–35] Such resistive-type modes appear in simple models without ionization or electron diffusion. The main feature of resistive modes is a strong dependence of growth rate and frequency on the electron mobility (resistivity).[34] Similar features are shown in this work, while the low-frequency mode (breathing mode) has weak or no dependency on the electron mobility; see Appendix A.

In fact, the frequency of resistive modes can vary significantly, ranging 0.1–10 MHz, and may become close to that of the breathing modes at the lower end of its spectrum. Some axial thruster models with ionization but without electron diffusion[1,36] claimed that these modes might be responsible for the breathing modes observed in Hall thrusters. For clarity, here, we will call breathing modes only those associated with atom depletion, whose frequencies scale according to atom fly-by time and ionization processes.

In our earlier work, we have proposed a reduced model (only ion and atom dynamics included) for the second, solo regime of the breathing mode. In this regime, the instability is triggered by the ion backflow (negative ion velocity) in the near-anode presheath region.[13] It was demonstrated that such configuration is prone to low-frequency oscillations, where the ion backflow region

is necessary. Recently, a similar conclusion has been reached in Ref. 37 where it was formally proved that the sign-alternating ion velocity profile with a positive slope, i.e., negative ion velocity near the anode and positive toward the exit, indeed is a necessary condition for the excitation the oscillations.

Another important result is the demonstration of the effect of atom temperature in the solo regime. We find that a finite energy spread of injected atoms strongly suppresses the amplitude of the oscillations compared to the injection cases with the same velocity, further called as monokinetic injection. It is found that even a small spread in the atom temperature for the solo regime notably lowers the amplitude of the breathing mode. For the first regime, with the presence of resistive modes, the atom temperature effect is negligible. We also show the role of ion heating (due to the resistive modes) and selective ionization of neutrals.

This paper is organized as follows. In Sec. II, a detailed description of both fluid and hybrid models is given. Section III defines the main features of two distinct regimes of low-frequency oscillations and presents results for the three test cases with a detailed comparison between the models.

II. FLUID AND HYBRID MODELS OF LOW-FREQUENCY DYNAMICS

This section presents a detailed description of the full fluid model and the hybrid model. Two models share the same electron fluid equations (drift-diffusion approximation and energy evolution). The models are considered in the electrostatic and quasi-neutral approximation, with the three species: neutral atoms, ions, and electrons. The ionization effects included via the electron–atom collisions, serving as a mechanism for supporting plasma discharge. Atom losses are only due to ionization, and radial atom losses were not included. The models also include the self-consistent electric field, the anode plasma recombination, the electron pressure effects, and the electron heat flux across the magnetic field.

The simulated length of 5 cm is assumed in the axial direction of a Hall thruster (x-direction), with the channel exit in the middle where the radial magnetic field has its maximum, Fig. 1. The profile of the magnetic field magnitude given by $B = B_0 \exp\left[-(x - x_0)^2/2\delta_B^2\right]$, where $x_0 = 2.5$ cm is the channel exit location and δ_B is the characteristic width coefficient for the magnetic field profile, which are set $\delta_{B,\text{in}} = 1.1$ cm, $\delta_{B,\text{out}} = 1.8$ cm, respectively, for the inner and outer regions, according to the LANDMARK setup.[32] The chosen magnetic field profile corresponds to a typical radial magnetic field of the SPT 100 thruster,[1,19,21] with the maximum near the channel exit.

A. Fluid model

First, a short description of each species dynamics is given, and then the full system of time-dependent equations is formulated. For the neutral atoms, a constant flow velocity V_a along the channel is considered, and the continuity equation with the source term is used to describe their dynamics,

$$\frac{\partial n_a}{\partial t} + V_a \frac{\partial n_a}{\partial x} = -\beta n_a n_e, \tag{1}$$

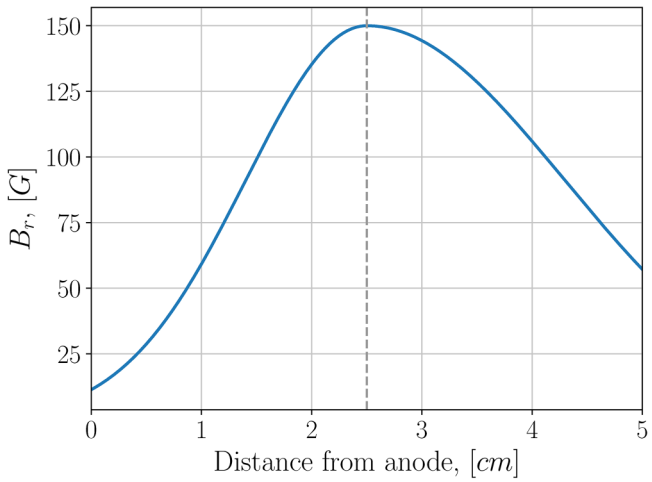

FIG. 1. The magnetic field profile used in simulations, with the channel exit located at the middle, 2.5 cm from the anode (dashed line).

where n_a is the atom number density, n_e is the electron number density, and $\beta(\varepsilon)$ is the ionization rate coefficient that depends on the electron energy $\varepsilon = (3/2)T_e$, where T_e is the electron temperature (β is shown in Appendix B). The ionization due to electron-atom impact produces a pair of ions and electrons with a loss of neutral atoms, hence the sink term $-\beta n_a n_e$ (same and opposite sign source terms are included in the ion and electron continuity equations).

The ion species are unmagnetized (the gyroradius is much larger than the thruster dimensions for a typical magnitude of a magnetic field in the thruster) and described with the conservation of number density and momentum equations,

$$\frac{\partial n_i}{\partial t} + \frac{\partial}{\partial x}(n_i V_i) = \beta n_a n_e, \tag{2}$$

$$\frac{\partial V_i}{\partial t} + V_i \frac{\partial V_i}{\partial x} = \frac{e}{m_i} E + \beta n_a (V_a - V_i), \tag{3}$$

where n_i is the ion density, V_i is the ion flow velocity, E is the axial electric field, e is the scalar elementary charge, and m_i is the ion mass (Xenon, 131.293 amu). The ion pressure term and the generalized viscosity tensor are neglected in this model (ions are ballistic with temperatures much lower than that of an electron component). Note that the radial sheath losses are often included in low-frequency models of a Hall thruster.[21] Such losses are of the same order of magnitude as the ionization losses. We neglect this effect in the present study, focusing on the main coupling mechanism between ions and neutrals, such as the ionization and the recombination at the anode.

The magnetized electron species are described with the first three fluid moment equations (electron inertia is neglected):

$$\frac{\partial n_e}{\partial t} + \frac{\partial}{\partial x}(n_e V_{ex}) = \beta n_a n_e, \tag{4}$$

$$0 = -\frac{e}{m_e}\mathbf{E} - \frac{eB}{m_e}(\mathbf{V}_{e\perp} \times \hat{\mathbf{z}}) - \frac{1}{n_e m_e}\frac{\partial(n_e T_e)}{\partial x} - \nu_m \mathbf{V}_{e\perp}, \quad (5)$$

$$\frac{3}{2}\frac{\partial}{\partial t}(nT_e) + \frac{5}{2}\frac{\partial}{\partial x}(n_e V_{ex} T_e) + \frac{\partial q_e}{\partial x} = -n_e V_{ex}\frac{\partial \phi}{\partial x} - n_e n_a \mathrm{K} - n\mathrm{W}, \quad (6)$$

where n_e is the electron density, $\mathbf{V}_{e\perp} = (V_{ex}, V_{e\theta})$ is the electron flow velocity perpendicular to the magnetic field (x and θ are the axial and the azimuthal coordinates), m_e is the electron mass, B is the external radial magnetic field, ν_m is the total electron momentum exchange frequency, W is an anomalous energy loss coefficient, K is the collisional energy loss coefficient (it is shown in Appendix B), and q_e is the electron heat flux. A phenomenological anomalous electron energy loss coefficient (e.g., due to radial sheath losses) W is introduced[19] as

$$\mathrm{W} = \nu_\varepsilon \varepsilon \exp(-U/\varepsilon), \quad (7)$$

where $\varepsilon = 3T_e/2$, $U = 20\,\mathrm{eV}$ and ν_ε is the anomalous energy loss frequency. The range of $\nu_\varepsilon = (0.3{-}1.4) \times 10^7\ \mathrm{s}^{-1}$ is found to adequately reproduce experimentally observed electron temperature profiles, with the average peak electron temperature in the range (24–38) eV.

The heat flux across the magnetic field is

$$q_e = -\frac{5}{2}\mu_e n T_e \frac{\partial T_e}{\partial x}. \quad (8)$$

The electron momentum conservation equation (5) is simplified assuming no pressure gradients or equilibrium electric fields other than in the axial direction; hence, the axial electron velocity (denoted further as V_e) can be expressed as

$$V_e = -\mu_e E - \frac{\mu_e}{n_e}\frac{\partial(nT_e)}{\partial x}, \quad (9)$$

where the electron mobility μ_e is the well-known classical electron mobility across the magnetic field,

$$\mu_e = \frac{e}{m_e \nu_m}\frac{1}{1 + \omega_{ce}^2/\nu_m^2}, \quad (10)$$

where $\omega_{ce} = eB/m_e$ is the electron cyclotron frequency. Equation (9) is commonly called the drift-diffusion equation. The model of electron transport is based on the assumption of the following total electron momentum exchange collision frequency:

$$\nu_m = \nu_{en} + \nu_{walls} + \nu_B, \quad (11)$$

where electron-neutral collision frequency ν_{en}, electron-wall collision frequency ν_{walls}, and anomalous Bohm frequency ν_B are given with

$$\nu_{en} = k_m n_a, \quad (12)$$

$$\nu_{walls} = \alpha 10^7\ (\mathrm{s}^{-1}), \quad (13)$$

$$\nu_B = (\beta_a/16)eB/m_e, \quad (14)$$

where $k_m = 2.5 \times 10^{-13}\ \mathrm{m}^{-3}\ \mathrm{s}^{-1}$ and α and β_a are free parameters. For the electron mobility model, different parameters are used inside and outside the channel (denoted additionally as *in*, *out*): the near wall conductivity contribution $\alpha_{\mathrm{in}} = 1$, $\alpha_{\mathrm{out}} = 0$, and the anomalous contribution is set to $\beta_{a,\mathrm{in}} = 0.1$, $\beta_{a,\mathrm{out}} = 1$. The anomalous loss (electron) energy frequency coefficient in Eq. (7) is a constant, set to $\nu_{\varepsilon,\mathrm{out}} = 10^7\ \mathrm{s}^{-1}$ outside the channel. Inside the channel, $\nu_{\varepsilon,\mathrm{in}}$ is variable and serves as the input parameter of the model; see Sec. III.

The step-like behavior of some model parameters (inside and outside the channel) can lead to numerical difficulties, but the obtained results were tested for convergence and the main behavior is reproduced in both models (fluid and hybrid). Moreover, the fluid model implemented in the BOUT++ was tested against the fluid code MAGNIS[38–40] for the same model resulting in a perfect match between two. Numerical details and convergence tests for the fluid model are presented in Appendix C.

Here, we seek the low-frequency and bulk plasma modes; thus, electron inertia is neglected (as shown above), and furthermore, the full plasma quasineutrality is assumed. One can check the validity of the quasi-neutral approximation[17] using the Poisson equation $\varepsilon_0 \partial E/\partial x = e(n_i - n_e)$ (ε_0 is the permittivity of free space). With the typical values of the electric field $E \approx 10^4\,\mathrm{V/m}$, the size of acceleration zone $\approx$1 cm, and average plasma density $n_0 = 10^{17}\ \mathrm{m}^{-3}$, one obtains the difference $(n_i - n_e)/n_0 \approx 5 \times 10^{-4}$. Instead of the Poisson equation, the electric field is found from the electron momentum equation as shown below. Note that while the quasineutrality neglects a potential drop in the Debye sheath near the anode, it still allows the presheath region to form if the electron pressure is included,[41–44] as in our electron model. The presheath is the region where the electric field is induced to accelerate ions toward a plasma boundary to compensate the electron current due to the pressure gradient. An alternative to the fully quasi-neutral approach used in this paper is solving the Poisson equation with implicit (or semi-implicit) methods, which allows one to ignore the Debye length scales since full resolution of Debye scales would be excessive for the large-scale problems presented in this paper. A possible advantage of implicit approach is the resolution of the Debye sheath (although approximately), where the sheath potential drops over one computational cell, assuming that the cell size is larger than the Debye length.[45] We believe that bulk oscillations in Hall thruster, which is the main object of this study, are well reproduced with the full quasi-neutral approach given above.

The full system of time-dependent fluid equations to be solved includes Eqs. (1), (2), (3), and (6), along with the drift-diffusion form for the electron velocity equation (9). Full quasineutrality $n = n_i = n_e$ is enforced, and the self-consistent electric field is found via the electron drift-diffusion Eq. (9), given by

$$E = \frac{J_T}{en\mu_e} - \frac{V_i}{\mu_e} - \frac{1}{n}\frac{\partial n T_e}{\partial x}, \quad (15)$$

where the total current density $J_T = en(V_i - V_e)$. Here, J_T is constant in space (divergenceless current), which can be seen by combining continuity equations for ions and electrons with quasi-neutral assumption. We will use the integral approach, consisting

of the evaluation of the total current density J_T via the constraint $\int_0^L E dx = U_0$ [then, it is substituted to Eq. (15) to evaluate the electric field], which yields

$$J_T = \frac{U_0 + \int_0^L \left(\frac{V_i}{\mu_e} + \frac{1}{n}\frac{\partial p_e}{\partial x}\right) dx}{\int_0^L \frac{dx}{en\mu_e}}, \tag{16}$$

where L is the system length and $U_0 = 300$ V is the applied voltage (without the sheath voltage). In this model, the effects of external circuit and fluctuations of the applied voltage are not included.

The fluid model is solved with the following boundary conditions. A constant mass-flow rate $\dot{m} = 5\,\mathrm{mg\,s^{-1}}$ and the full recombination of plasma that flows to the anode determines the value of n_a at the anode boundary,

$$n_a(t, x = 0) = n_{a0} + n_{a,\mathrm{rec}} = \frac{\dot{m}}{m_i A V_a} - \frac{n_i V_i(t, x = 0)}{V_a}, \tag{17}$$

where $A = \pi(R_2^2 - R_1^2)$ is the anode surface area, with the inner and outer radii $R_1 = 3.5$ cm and $R_2 = 5$ cm. The value of the ion velocity is imposed at the anode as $V_i(t, x = 0) = -b_v\sqrt{T_e/m_i}$ with the parameter $b_v = 0{-}1$, the Bohm velocity factor that can be varied. Furthermore, we show that Case 2 is highly sensitive to the parameter b_v, and other cases are insensitive. In general, the electron energy balance (6) with the heat flux included requires two boundary conditions. The electron temperature near the anode observed in experiments[43,44] is of a few electron volts; thus, we have fixed both anode and cathode electron temperatures to $T_e(t, x = 0) = T_e(t, x = L) = 2$ eV to stay close to the experimental conditions.[43]

As noted in Ref. 17, plasma acceleration in the configuration of the axial direction of a Hall thruster shows similarities to the flow in a de Laval nozzle. Indeed, the whole acceleration region can be split into subsonic $V_i < c_s$ and supersonic $V_i > c_s$ regions, where $c_s = \sqrt{T_e/m_i}$ is the ion-sound speed. While in a de Laval nozzle, the transition through a sonic point happens at the region with the smallest cross section of the channel due to extrema condition and regularity requirement, for the bounded plasma configuration, the position is determined via the nonlinear relationship between plasma parameters (and their first derivative) at the sonic point and a value of the total current.[46] Note that the total current J_T, given by Eq. (16), is a function of U_0 with the integral dependence on all main plasma parameters; thus, the problem is inherently nonlocal, which has no analogy with the standard de Laval nozzle. Another difference is that in the axial direction of Hall thrusters, the presheath region can induce the backward ion flow in a large portion of the thruster channel (see Case 2 below).

B. Hybrid model

The hybrid model has the same electron equations as in the fluid model, while ions and neutrals are modeled via a particle-in-cell (PIC) method.[18,30,31] The plasma recombination effect is also included via the relationship (17), but the ion velocity at the anode is not forced to satisfy the Bohm velocity. The ionization is included via the electron–atom impact with the Monte Carlo sampling of ionization events (via the null collision method[45,47]) using the macroscopic ionization rate $\beta(\varepsilon)$, obtained in the same way as in the fluid model. Neutral atoms are injected with a constant flow rate $\dot{m}$ either with the constant velocity V_a (monokinetic), thus, $f(v_x) = \delta(v_x - V_a)$, or with a half-Maxwellian velocity distribution function at the left wall (anode),

$$f(v_x) = \frac{2v_x}{v_{Ta}^2}\exp\left(-\frac{v_x^2}{v_{Ta}^2}\right), \quad v_x > 0, \tag{18}$$

where $v_{Ta}^2 = 2k_B T_a/m_a$ is the atom thermal speed ($m_a = m_i$) and T_a is the atom temperature (in K). For the half-Maxwellian injection (18), the average flow velocity is $v_{Ta}/\sqrt{\pi}$. Ions are assumed singly charged and unmagnetized; thus, they are only accelerated by an electric field. Ions are produced according to the ionization rate coefficient $\beta(\varepsilon)$, i.e., self-consistently with the electron temperature evolution and the local atom density. Both atoms and ions are lost at the boundaries. In this model, the ion velocity is not forced to the Bohm velocity, like in the fluid ion model. With the quasi-neutral approach ($n_e = n_i$ is forced at every time step), plasma density is evaluated from the ion particle distribution and thereafter used for the electron temperature (6) and the electric field (9) calculations. Formally, the evolution of the distribution function for ions $f_i(x, v_x, t)$ and atoms $f_a(x, v_x, t)$ is described with the Boltzmann equation for each species:

$$\frac{\partial f_i}{\partial t} + v_{ix}\frac{\partial f_i}{\partial x} + \frac{e}{m_i}E\frac{\partial f_i}{\partial v} = S(x, v_x), \tag{19}$$

$$\frac{\partial f_a}{\partial t} + v_{ax}\frac{\partial f_a}{\partial x} = -S(x, v_x), \tag{20}$$

where $S(x, v_x)$ is the collisional source term due to the ionization. In the case of the monokinetic target species (atoms), the ionization leads to the ion creation with the atom velocity V_a (constant) and the source term can be expressed[19] as $S(x, v_x) = \beta n_e n_a \delta(v_x - V_a)$. For the simulations with a finite atom temperature, newly created ions assigned velocities by sampling from the isotropic Maxwellian distribution with the temperature T_a with the standard sampling techniques.[48] Solutions to Eqs. (19) and (20) effectively obtained by solving the motion equations for the corresponding particle type (the method of characteristics via a PIC method). Equations (19) and (20) and the electron fluid equations (6) and (9) form a complete set of equations solved in the hybrid model.

In the hybrid model, in all test cases presented below, the average total number of macroparticles in the system was $\approx 5 \times 10^6$ for the ions and $\approx 0.5 \times 10^6$ for the atoms. The fluid equations (for electrons) in the hybrid model are resolved with the finite volume methods,[45] with the same spatial discretization and the time step as the PIC method, set to 300 cells and $\Delta t = \Delta x/v_{\max}$, where $v_{\max} = 5\sqrt{2eU_0/m_i}$, resulting in $\Delta t = 1.62$ ns for $U_0 = 300$ V. The same time step is used as the collisional time step in the Monte Carlo process, and for a given Δt, the condition $\nu_{\mathrm{ion}}\Delta t \ll 1$ is well satisfied for a typical value of the ionization frequency $\nu_{\mathrm{ion}} \approx 5 \times 10^5\,\mathrm{s^{-1}}$ ($T_e = 20$ eV, $n_a = 10^{19}\,\mathrm{m^{-3}}$).

III. SIMULATION RESULTS AND COMPARISON

The fluid and the hybrid models described above were studied for three test cases (denoted as Cases 1, 2, and 3). Cases 1 and 2 will demonstrate two distinct regimes of low-frequency oscillations, and Case 3 shows the effect of atom temperature. Note that Cases 1 and 2 use monokinetic atoms with the velocity $V_a = 150\,\mathrm{m/s}$. Cases 1 and 2 are chosen with the following observation: larger values of anomalous (electron) energy loss frequency $\nu_{\varepsilon,\mathrm{in}}$ in Eq. (7) allow the high frequency (of ion fly-by time) modes to appear and coexist with the low-frequency modes, represented in Case 1. The simulations with lower values of $\nu_{\varepsilon,\mathrm{in}}$ reveal only the large amplitude low-frequency oscillations, and we call it the solo regime. In Case 1, $\nu_{\varepsilon,\mathrm{in}} = 0.95 \times 10^7\,\mathrm{s}^{-1}$, and in Case 2, $\nu_{\varepsilon,\mathrm{in}} = 0.4 \times 10^7\,\mathrm{s}^{-1}$. This is the only parameter distinguishing Cases 1 and 2 (for all cases reported in this paper, we keep $\nu_{\varepsilon,\mathrm{out}} = 10^7\,\mathrm{s}^{-1}$).

Besides the different time-dependent behavior, these regimes show a notable difference in the time-averaged axial profiles of the ion velocity and the electron energy; see Figs. 2(a) and 2(b). For Cases 1 and 2, the ion velocity profile is similar near the exit and beyond, but in the near-anode region, the ion backflow region (where ions are moving toward the anode) is much shorter for Case 1, Fig. 2(a). The ion backflow region is associated with the presheath formation near the anode (with the negative electric field). The size of the presheath region as a function of $\nu_{\varepsilon,\mathrm{in}}$ is shown in Fig. 3, where a transition between regimes with large and short backflow regions occurs near the value $\nu_{\varepsilon,\mathrm{in}} = 0.75 \times 10^7\,\mathrm{s}^{-1}$. The electron temperature for Case 2 is peaked near the channel exit, Fig. 2(b), with very low values in the near-anode region. For Case 1, the electron temperature spreads more uniformly and to the near-anode region.

The difference in the electron temperature distributions might be due to the difference in the electron flow velocity near the anode. Figure 4 shows the time-averaged electron velocity components, evaluated according to Eq. (9). Note a substantially higher electron velocity due to the pressure gradient in Case 1 for $x < 0.4\,\mathrm{cm}$, which also results in a larger total electron flow velocity near the anode. Thus, in Case 1, convection reduces the electron temperature in the ionization region (increasing it near the anode). Indeed, the average gradient parameter $L_n^{-1} = \partial_x n_i / n_i$ is about five times larger for Case 1, which drives this electron current. Recall that the presheath region is formed due to diffusive electron current by inducing ion current (total current is conserved), generating the negative electric field in this region. All features presented above clearly distinguish Case 1 and Case 2.

Finally, Case 3 demonstrates the effect of a finite atom temperature, where atoms are injected into the system with the

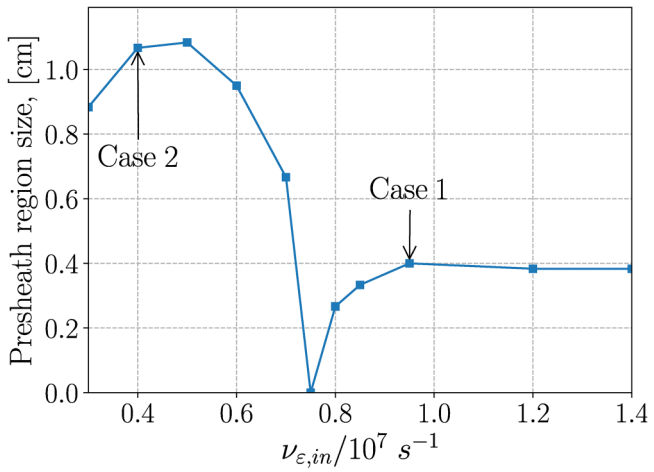

FIG. 3. Extent of the presheath zone, defined as the region with a negative electric field near the anode as a function of anomalous electron energy loss coefficient ν_ε (result obtained with the hybrid model). The range of ν_ε shown here is found to correspond adequately to the electron temperature profiles observed in experiments. For example, for values $\nu_\varepsilon < 0.3 \times 10^7\,\mathrm{s}^{-1}$, the peak electron temperature reaches values of higher than 50 eV.

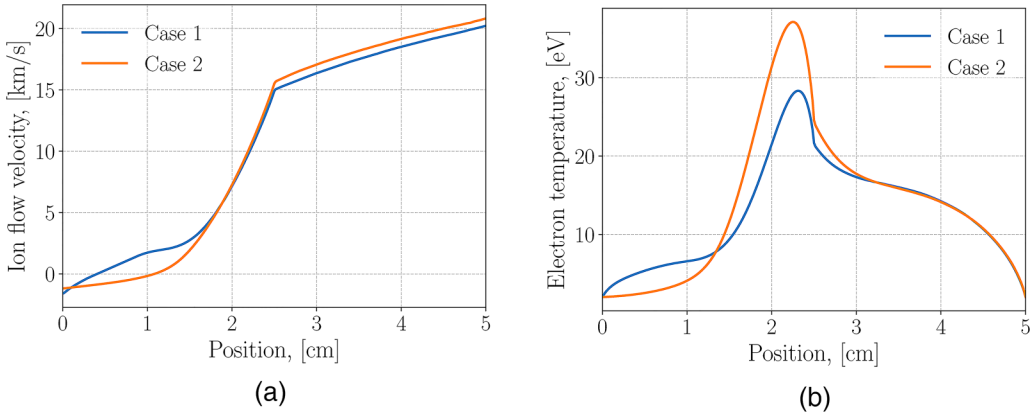

FIG. 2. Averaged in time profiles of ion velocity (a) and electron temperature (b) for Case 1 ($\nu_{\varepsilon,\mathrm{in}} = 0.95 \times 10^7\,\mathrm{s}^{-1}$) and Case 2 ($\nu_{\varepsilon,\mathrm{in}} = 0.4 \times 10^7\,\mathrm{s}^{-1}$). The result is obtained with the hybrid model.

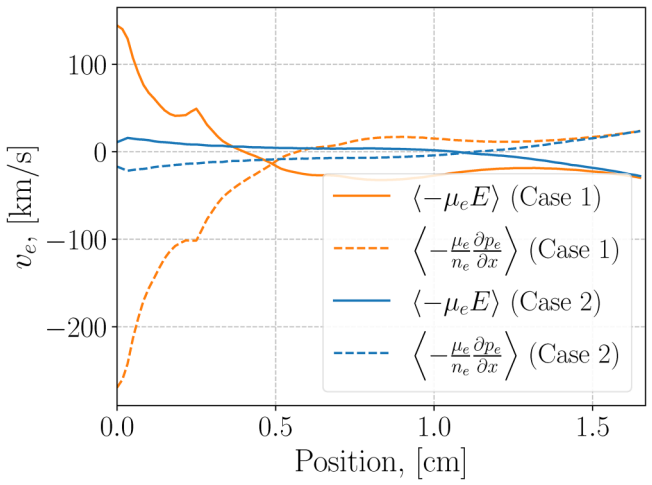

FIG. 4. Electron flow velocity components given by Eq. (9) for Cases 1 and 2, averaged in time (denoted with angle brackets) over few periods of the low-frequency component (result obtained with the hybrid model).

half-Maxwellian distribution, Eq. (18), and all the other parameters are the same as in Case 2. The main effect of atom temperature is found to be a significant reduction of a breathing mode amplitude to those observed in Case 2. Besides a finite atom temperature, all parameters for Case 3 are exactly the same as in Case 2, and the atom temperature is set to $T_a = 500\,\mathrm{K}$ ($V_a = 142\,\mathrm{m/s}$, close to monokinetic 150 m/s used in Cases 1 and 2).

A. Case 1: High electron energy losses: The co-existence of low- and high-frequency modes

This case exhibits both low- and high-frequency oscillations in the fluid and hybrid models. The hybrid model results in a smaller amplitude of the total current; see Figs. 5(a) and 5(b). The time-averaged total currents are close, 8.2 A in the hybrid model and 8.3 A in the fluid model. The ratio of the time-averaged ion current (at the plume exit, $x = 5\,\mathrm{cm}$) to the total current is 45% in the hybrid model and 48% in the fluid.

The spectral power of the total current also shows some differences in both low- and high-frequency ranges, Figs. 6(a) and 6(b). The main low-frequency mode in the fluid model is 11.4 kHz, while it is 14.4 kHz in the hybrid model. The total current signal in the hybrid model contains more noise (statistical noise due to the use of macroparticles), but the high-frequency component is clearly seen at around 125 kHz. In the fluid model, the high-frequency mode is shifted toward higher frequencies, centered at about 175 kHz.

Besides the currents, a more rigorous comparison between the two models is shown in Figs. 7(a)–7(d), with the time-averaged axial profiles of the main plasma quantities. Due to the oscillatory nature of these solutions, the averaging time window was chosen as the ten periods of the corresponding main low-frequency mode in each simulation. The main discrepancy lies in the peak plasma density in the ionization (source) region at about 1.3 cm from the anode; the hybrid model results in a higher value of the peak plasma density. Also, the ion velocity in the plume ($x > 2.5\,\mathrm{cm}$) is slightly higher in the hybrid model.

The ion phase space (hybrid model) is shown in Fig. 8(a). The ion velocity distribution function (IVDF) is highly inhomogeneous

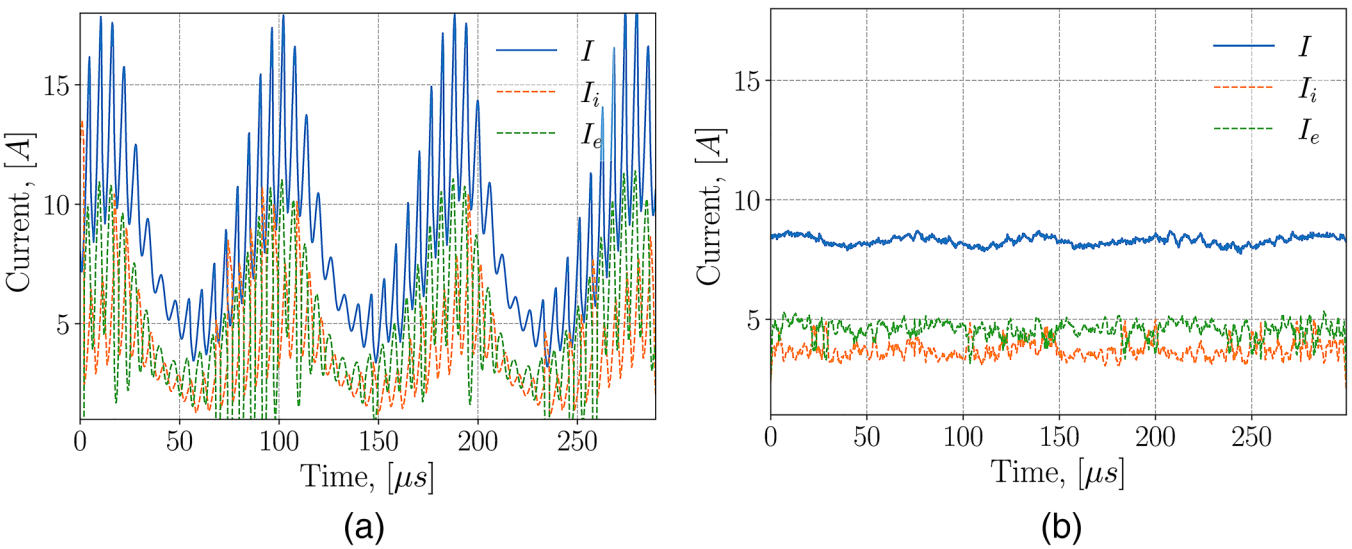

FIG. 5. Amplitudes of the total, ion, and electron currents in the fluid model (a) and the hybrid model (b). Ion and electron currents are evaluated at $x = 5\,\mathrm{cm}$. Note that electron current fluctuations can become negative (electrons turned back to cathode) for a short instance of time when the electron diffusion term becomes larger than the drift term, Eq. (9). A small averaging window of length 2.3 μs is applied to the ion and electron currents (to filter out high-frequency noise).

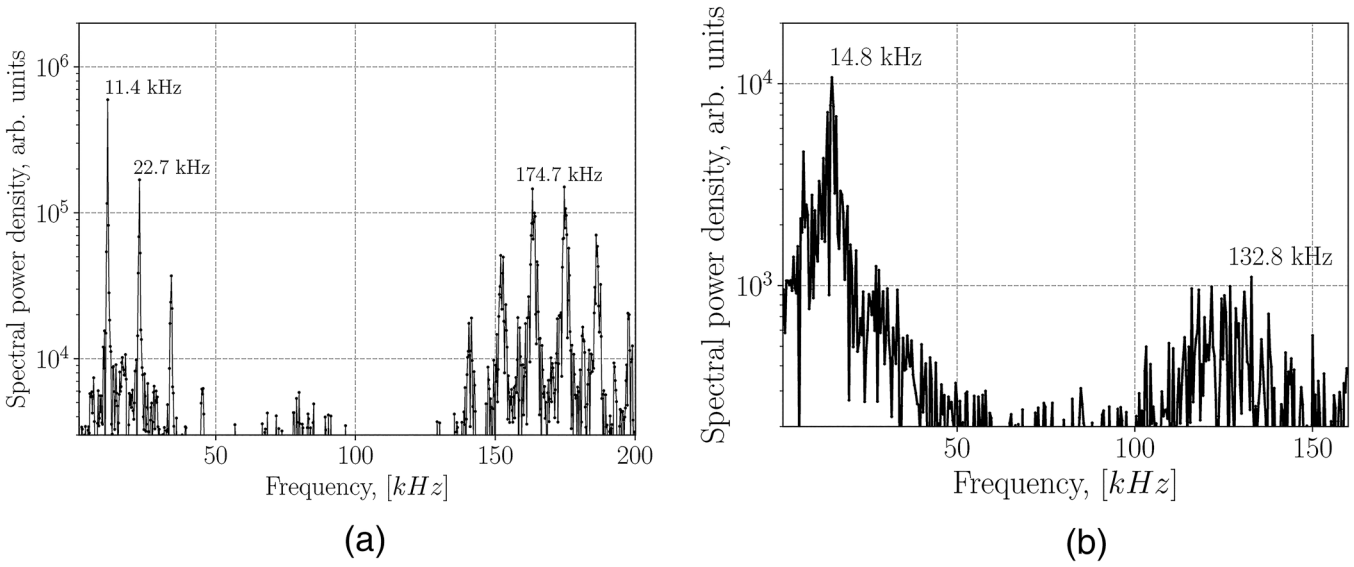

FIG. 6. Spectral density of the total current yield in the fluid model (a) and the hybrid model (b).

inside the channel, suggesting that the higher fluid moments may play a role (recall that the nullified pressure term gives the closure in the ion fluid model). Typically, ion pressure effects are neglected due to a low ion temperature; ion formation is due to the ionization process as they carry the low atom temperature even when accelerating by the axial electric field.

To check the validity of this assumption, the fluid moments were calculated from the kinetic particle representation in the hybrid model. It allows to test the ion momentum balance equation (to identify the role of the ion pressure term) in a more complete form,

$$\frac{\partial V_i}{\partial t} + V_i \frac{\partial V_i}{\partial x} = \frac{e}{m_i} E - \frac{1}{n_i} \frac{\partial p_i}{\partial x} + \beta n_a (V_a - V_i), \tag{21}$$

where the fluid moments, such as the ion density n_i, the ion flow velocity V_i, and the ion pressure p_i, were evaluated from the ion distribution function in the following way:

$$n_i = \int f_i \, dv_{ix}, \tag{22}$$

$$V_i = \frac{1}{n_i} \int v_i f_i \, dv_{ix}, \tag{23}$$

$$p_i = m_i \int v_i' v_i' f_i \, dv_{ix}, \tag{24}$$

where $v_i' = v_i - V_i$ is the random component of the particle velocity. The time-averaged profile of the ion temperature $T_i = p_i/n_i$ is shown in Fig. 8(b), revealing values of the ion temperature up to 3.5 eV in the ionization region, with the average over the whole domain of 1.7 eV. For the momentum balance test, each term in Eq. (21) was evaluated as a function of time and space and then averaged in time over a few periods of the main low-frequency mode. Figure 9(a) shows the difference between the left- and right-hand sides of Eq. (21). The plotted terms were normalized to the value V^2/L, where the ballistic ion velocity is $V^2 = 2eU_0/m_i$ with the potential difference $U_0 = 300$ V over the system length L. It is seen that the ion pressure term notably improves the overall ion momentum balance, suggesting that the fluid model for this configuration should not ignore the ion pressure.

It is interesting to further inspect each term in Eq. (21). The unsteady term $\partial V_i/\partial t$ is negligible due to time averaging, while the other terms have comparable values inside the channel; see Fig. 9(b). In the near-anode region, the ion pressure ($T_i \approx 0.1$ eV) and the ionization friction are negligible; therefore, the ions accelerate toward the anode in the weak negative electric field ballistically. Then, in the ionization (source) region, we see that all terms are comparable. The ion pressure and the collisional drag compensate the ballistic acceleration; therefore, the ion inertia remains low. Finally, in the acceleration zone ($x > 1.5$ cm) and beyond, the inertial and ballistic terms start to dominate. It is seen that the ion pressure term changes the sign at $x \approx 1.6$ cm [due to ion density profile, Fig. 7(b)] and contributes to the ion acceleration.

Based on the results above, the ion pressure force term $-T_i \partial_x n_i$ was added to the fluid model with the temperature kept constant for simplicity. For the self-consistent treatment, an ion energy balance equation shall be included (or equation of state). The average in space and time value of the ion temperature evaluated in the hybrid model for this case is 1.7 eV. However, it is found to damp the oscillations and produce a fully stationary

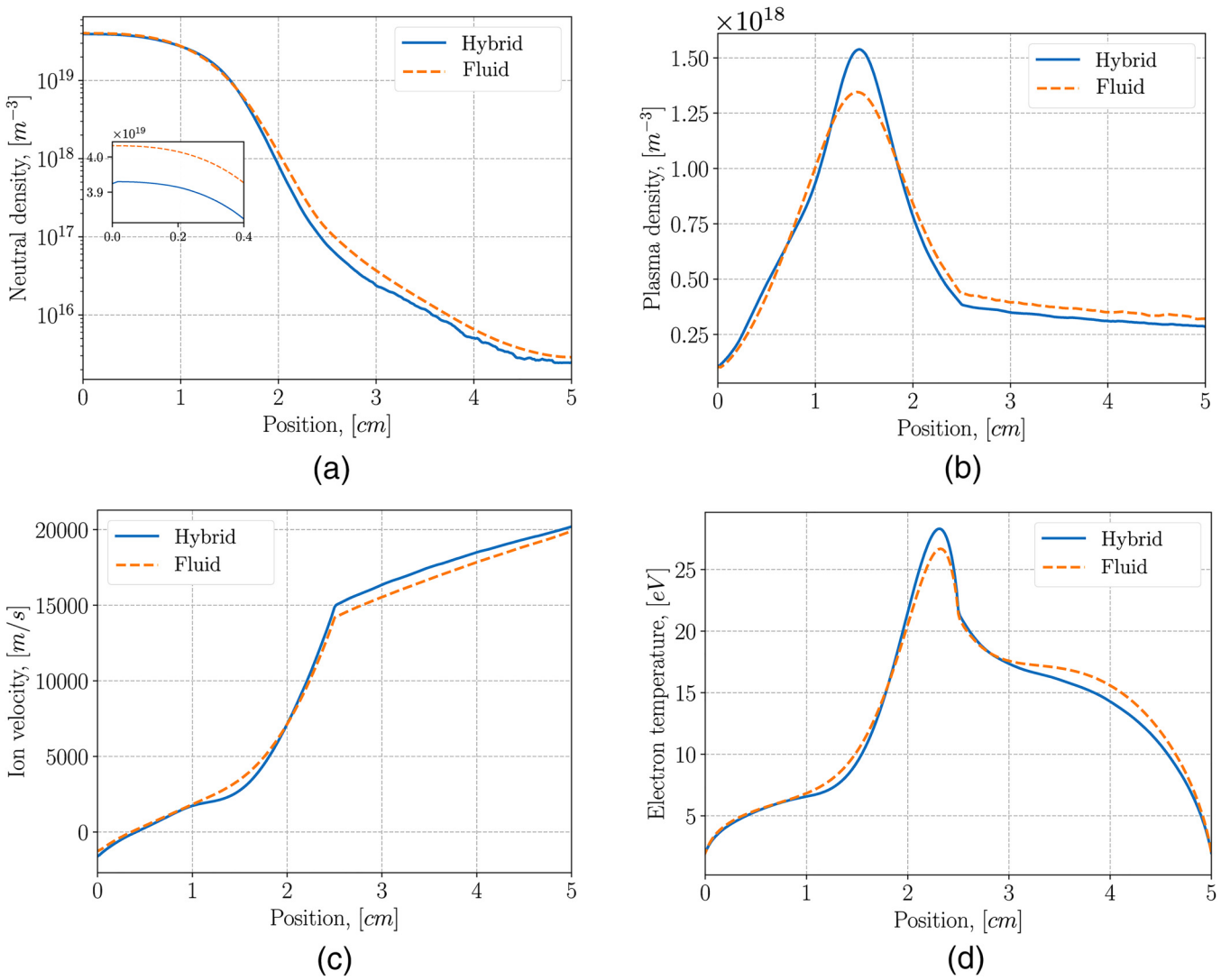

FIG. 7. Comparison of time-averaged axial macroscopic profiles resulted from fluid and hybrid models of neutral density (a), plasma density (b), ion flow velocity (c), and electron temperature (d) for Case 1.

solution with the ion pressure force mentioned above. With a lower value of $T_i = 1.2$ eV, the oscillatory solution is obtained. This results in a better agreement between the two models; the total current amplitude decreases and the main low-frequency mode increases [Figs. 10(a) and 10(b)]. The low-frequency mode increased to 13.9 kHz, and the high-frequency peak is shifted to a lower value of 153 kHz. The ratio of the ion current to the total current shows an improved agreement, 45%, the same as in the hybrid model. However, the time-averaged total current value of 8.7 A became somehow larger than in the hybrid model (8.2 A). Also, the higher frequency component is closer to the hybrid result. As for the peak plasma density discrepancy, Fig. 7(b), it remained similar.

B. Case 2: Low electron energy losses: The solo regime of the low-frequency mode

This case is subject to the low-frequency oscillations only, with the only difference to Case 1 in the value of the anomalous (electron) energy loss frequency, which is $\nu_{\varepsilon,\mathrm{in}} = 0.4 \times 10^7\ \mathrm{s}^{-1}$. As in the previous case, the total current amplitude is higher in the fluid model, Figs. 11(a) and 11(b), but the main oscillation frequency in two models is similar [Figs. 12(a) and 12(b)].

The time-averaged profiles agree well between the two models, with the only notable discrepancy in the plasma density profile, which is ≈30% lower inside the channel region for the fluid model; see Figs. 13(a)–13(d).

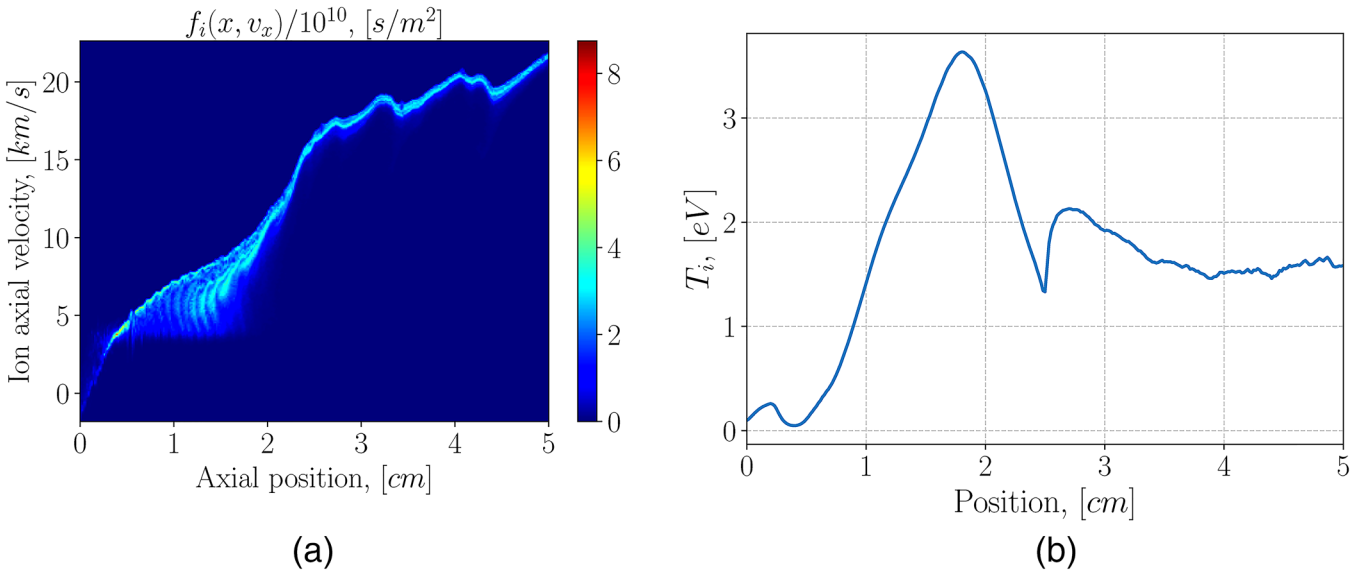

FIG. 8. Instantaneous image of the ion distribution function (in space of axial coordinate and axial velocity) in the hybrid model (a). Ion temperature spatial profile (time-averaged) evaluated from an ion kinetic representation in the hybrid model (b).

Unlike in Case 1, the IVDF for this case [Fig. 14(a)] reveals that the ion population remains cold (everywhere except in the near-anode region), and the ion momentum balance must be well satisfied without the ion pressure term. This is seen in Fig. 14(b), where the ion pressure force remains low everywhere in the channel. In fact, in this case, the ballistic ion acceleration is more pronounced, dominating everywhere except the stall point ($V_i \approx 0$). Indeed, the average (space and time) ion temperature, calculated similarly as in Case 1 from the hybrid model, is 0.3 eV (about 5 times smaller than in Case 1) and not exceeding 1 eV in the domain.

The main stages of the breathing mode dynamics are illustrated with the plasma and atom density distributions at various moments in time (Fig. 15). After atoms reach the ionization zone and undergo ionization, plasma density increases and is quickly depleted (≈1 km/s) to the left (due to the backflow region with a

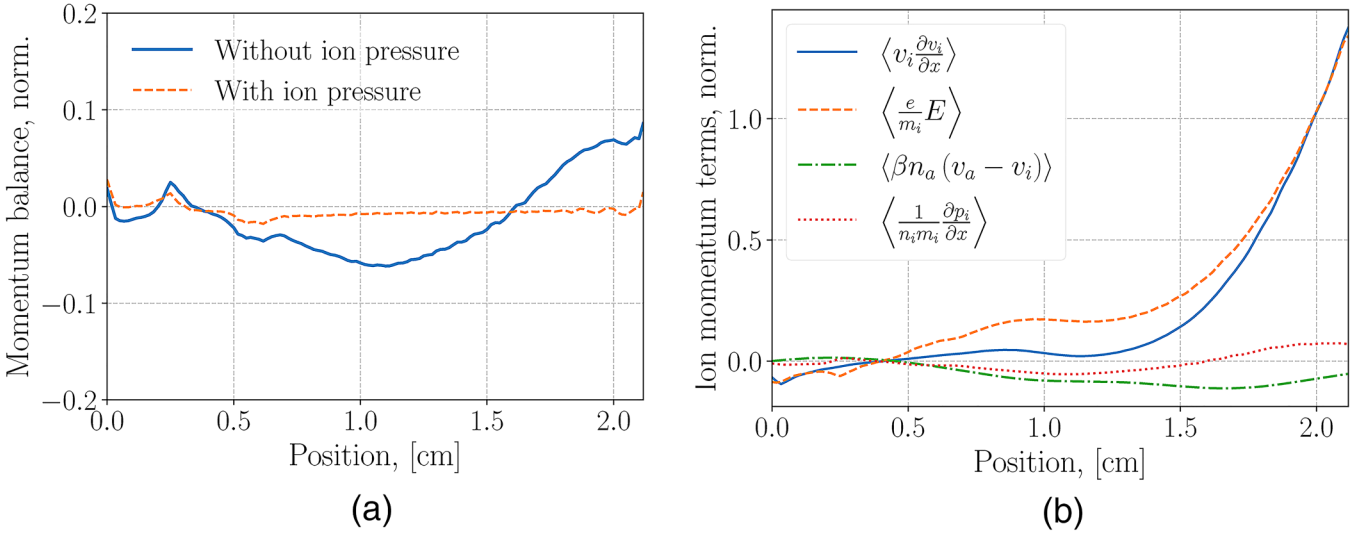

FIG. 9. Difference between left and right hand sides of the ion momentum balance equation (22) evaluated from the kinetic description of the hybrid model (a). Separate terms of the same equation averaged in time (denoted with angle brackets) over few periods of the low-frequency component (b).

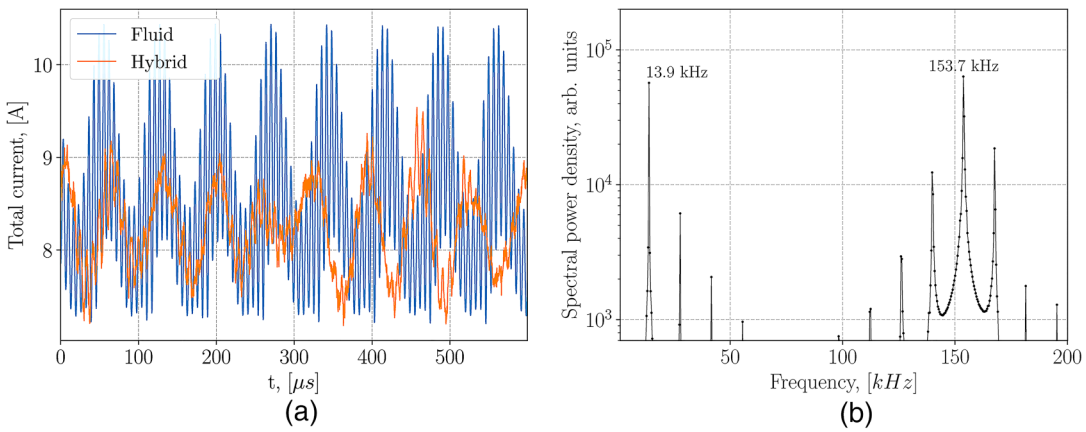

FIG. 10. Comparison of total current in the fluid model and the hybrid model (a) and the spectral power density of the total current in the fluid model (b). The result obtained is for the fluid model with the ion pressure term included.

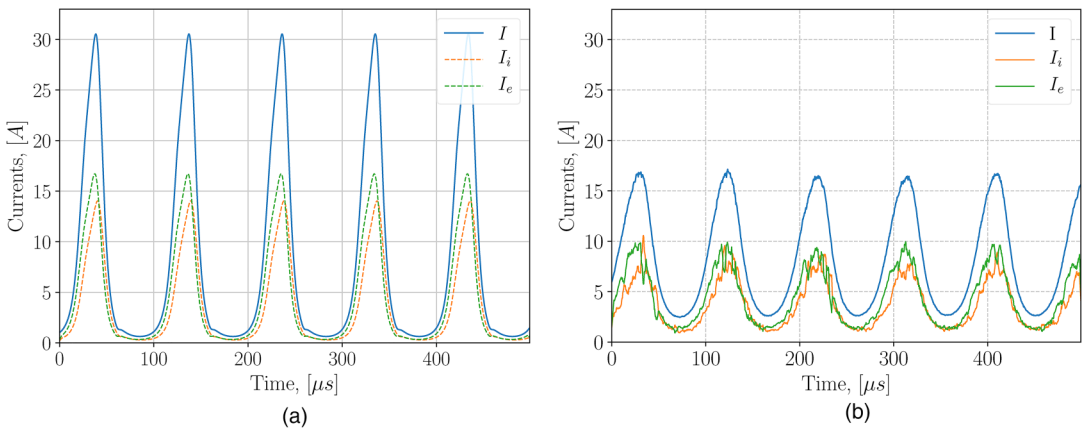

FIG. 11. Amplitudes of total, ion, and electron currents in the fluid model (a) and the hybrid model (b) for Case 2. Ion and electron currents are evaluated at $x = 5$ cm.

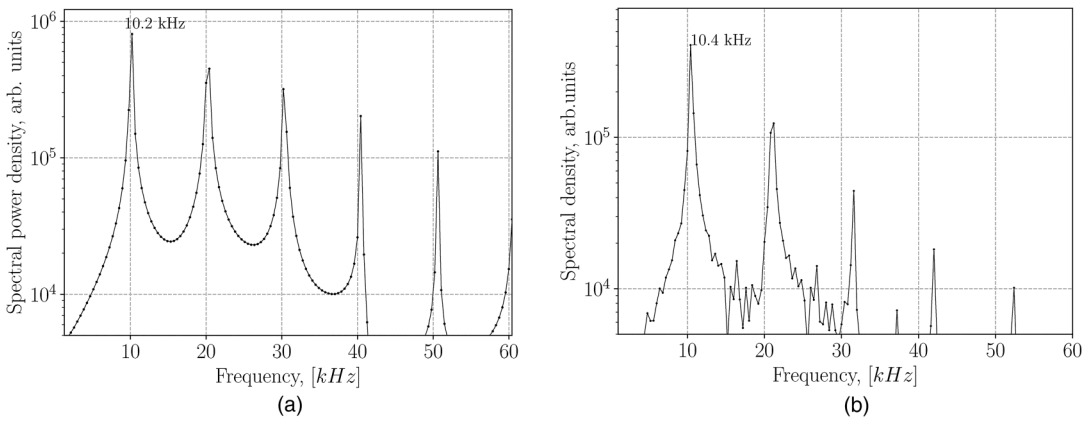

FIG. 12. Spectral density of the total current for the fluid model (a) and the hybrid model (b).

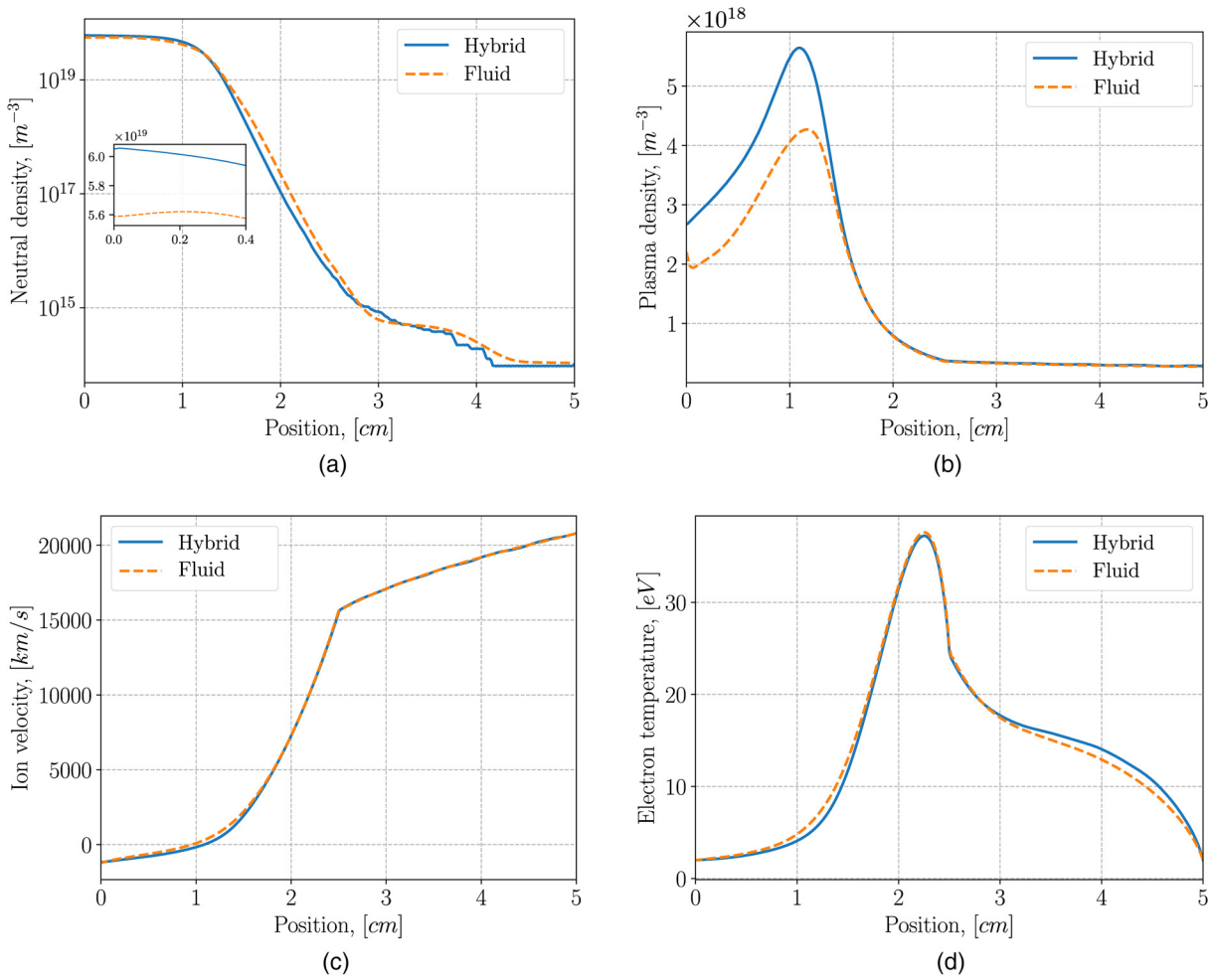

FIG. 13. Comparison of time-averaged axial macroscopic profiles resulted from fluid and hybrid models of neutral density (a), plasma density (b), ion flow velocity (c), and electron temperature (d) for Case 2.

negative ion velocity) and the right of the ionization zone. Then, all of the ion fluxes that reached the anode recombine and form the peak in the neutral density at the anode, increasing the number of atoms advecting to the ionization zone; this process repeats. In our previous work, Ref. 13, this setup was studied in detail with the reduced fluid model, consisting of the continuity equations for neutrals and ions with a prescribed ion velocity profile. It was shown that the ion backflow region near the anode is sufficient to excite the low-frequency oscillations, and the recombination is not necessary. The role of the recombination in this case consists of increasing the oscillation amplitude.

It is found that the oscillation dynamics in Case 2 highly depends on the recombination at the anode, modeled with Eq. (17), and the number of recombined atoms proportional to the oscillation current amplitude. Note that in Case 1, recombination plays a minor role and does not affect the presented results, which is seen in Fig. 16. In contrast, turning off the recombination in Case 2 nullifies the oscillations and the stationary solutions obtained (in both models). We suggest that the main difference in this case between the fluid and the hybrid model, in this case, lies in the differences with the ion velocity boundary condition. Normally, in the fluid quasi-neutral models, this boundary condition is fixed to the Bohm velocity, as in our fluid model.

When the Bohm boundary condition is scaled with the factor $b_v = 0-1$ (ion velocity effectively decreased at the anode) in the fluid model, the oscillation amplitude also decreases; see Fig. 17. It shows that the plasma recombination provides the additional feedback in this configuration, and the main difference with the hybrid model lies in the ion boundary conditions causing a larger oscillation amplitude in the fluid model. In the hybrid model, ions are not forced to satisfy the Bohm condition, and the flow velocity is established self-consistently. We modeled this behavior with the free boundary condition for the ion velocity at the anode in the fluid model, enforcing $\partial_x^2 V_i(t, x = 0) = 0$. In the presence

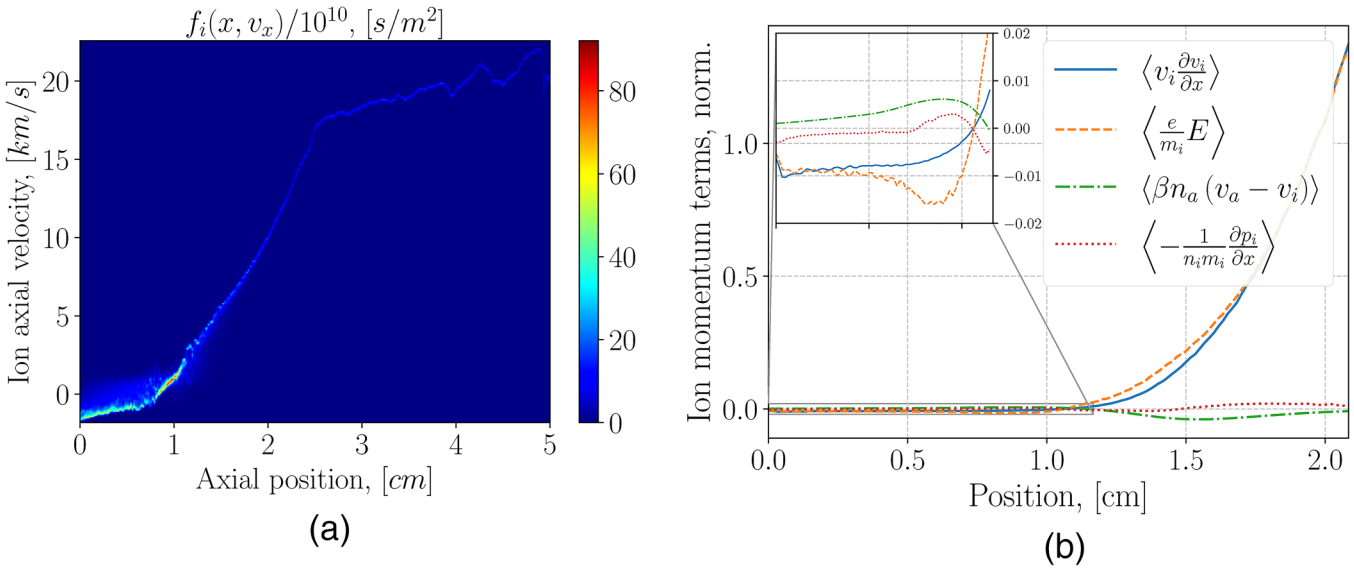

FIG. 14. Instantaneous image of the ion distribution function (in space of axial coordinate and axial velocity) in the hybrid model (a). Separate terms of the ion momentum balance equation (22) evaluated from the ion kinetic description (hybrid model), averaged in time (denoted with angle brackets) over few periods of the low-frequency component (b).

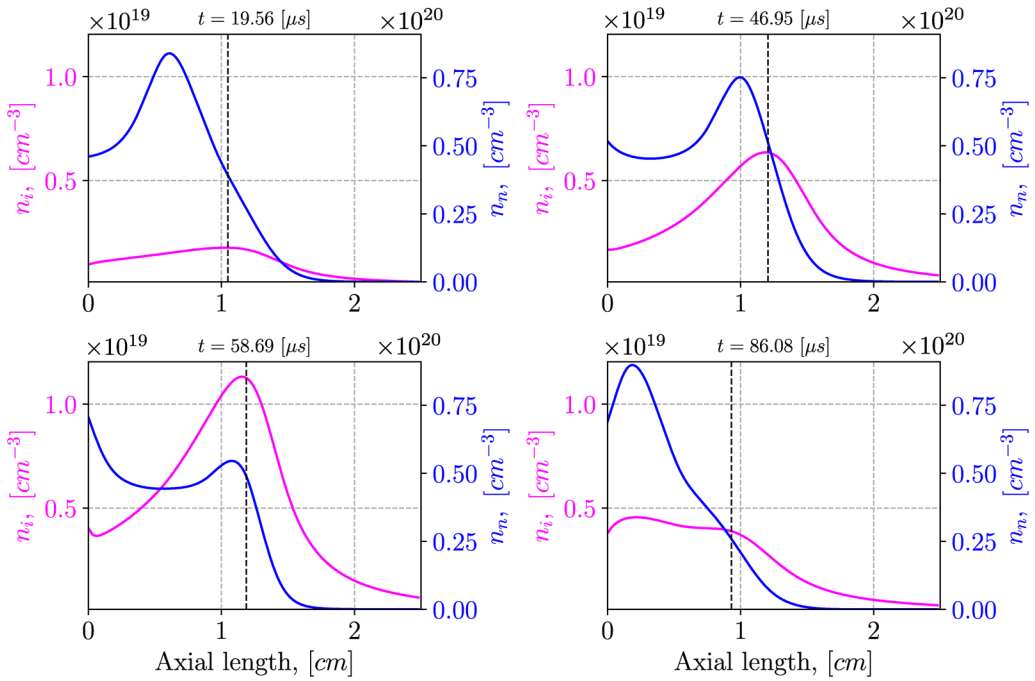

FIG. 15. Neutral and plasma density evolution during one oscillation period. The dashed line separates the region with negative (to the left) and positive (to the right) ion velocities.

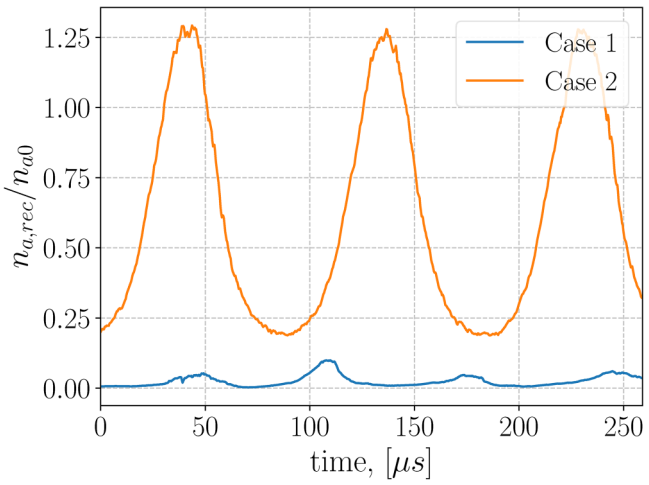

FIG. 16. Time-dependent value of recombined neutral density $n_{a,rec}$ at the anode, given by Eq. (17), for Case 1 and Case 2. It is normalized to the injected neutral density n_{a0} that corresponds to the mass-flow rate $\dot{m} = 5\,\mathrm{mgs}^{-1}$.

of ion backflow (like we see in Case 1,2) in the quasi-neutral approximation, the ion velocity at the anode is defined self-consistently by the characteristic at the location where $V_i = 0$; thus, a fixed boundary is not formally required. Moreover, depending on operating conditions, various sheath regimes can form in a Hall thruster;[43] thus, the ion velocity can differ from the Bohm velocity at the anode.

The obtained result in the fluid model with the free boundary condition for the ion velocity at the anode reveals less violent oscillations and generally better agrees with the hybrid

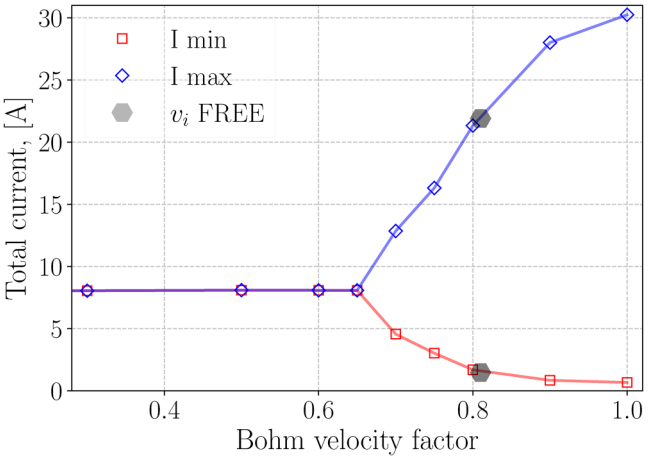

FIG. 17. Minimum and maximum total current values during oscillations for various ion velocities at the anode, expressed as fractions of the Bohm velocity. Note that oscillations are absent for $V_i < -0.65c_s$. The result is obtained with the fluid model.

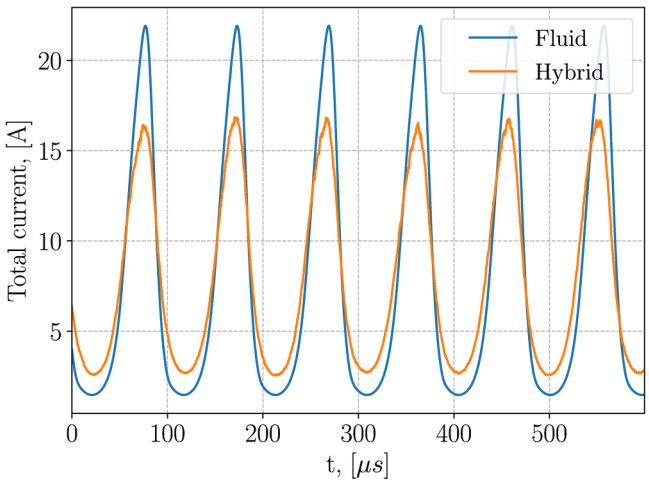

FIG. 18. Comparison of the total current obtained in both models where the free boundary condition used in the fluid model for ion velocity at the anode.

model results. The total current oscillation amplitude is lower, Fig. 18, closer to the hybrid mode result. The time-averaged atom and plasma density profiles are in a better agreement [Figs. 19(a) and 19(b)].

C. Case 3: Effects of finite temperature of neutral atoms

Here, the finite atom temperature is included, while all other parameters are kept as in Case 2. Atoms are injected at the anode with the half-Maxwellian flux distribution, Eq. (18), with temperature $T_a = 500$ K. Unlike Case 2, the oscillation amplitude in this case is much smaller in the hybrid model, with the amplitude of $\approx$1 A and the frequency of $\approx$18 kHz (in comparison with Case 2 with $\approx$13 A and $\approx$10.5 kHz), Figs. 21(a) and 22. In the previous cases, injected atoms in the hybrid model were kept monokinetic (zero thermal energy). The average injection velocity for the half-Maxwellian is $V_0 = v_{Ta}/\sqrt{\pi} = 142$ m/s, which is close to 150 m/s used in the previous monokinetic runs.

It was noticed that the atom flow velocity in the hybrid model exhibits a clear spatial dependence, "accelerating" along the channel. This effect is known as selective ionization (the ionization frequency does not depend on the atom particle velocity, but their mean free path does), observed both in experiments[49,50] and simulations.[51] It is clear that atoms in the fluid model with the simple advection equation (1) cannot capture this effect; hence, the atom momentum balance equation was included in the fluid model,

$$\frac{\partial(n_a V_a)}{\partial t} + \frac{\partial}{\partial x}\left(n_a V_a^2\right) = -\beta n_a n_i V_a - \frac{T_a}{m_i}\frac{\partial n_a}{\partial x}, \tag{25}$$

where the closure is given with the constant temperature $T_a = 500$ K. The illustration that the momentum balance given by Eq. (25) has a sufficient number of terms, the atom fluid moments were calculated from the kinetic representation of atoms in the hybrid model, and the balance is compared; see Fig. 20. Thus,

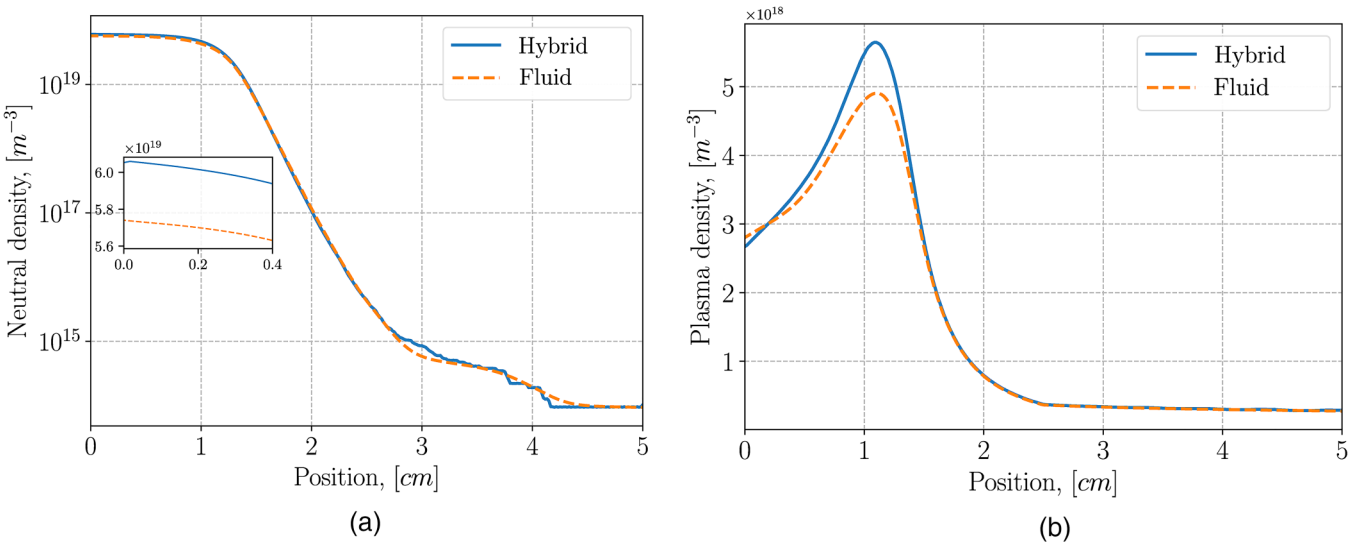

FIG. 19. Atom (a) and ion (b) axial profiles, averaged in time, compared in both models where the free boundary condition used in the fluid model.

Eq. (25) along with the continuity equation,

$$\frac{\partial n_a}{\partial t} + \frac{\partial (n_a V_a)}{\partial x} = -\beta n_a n_i, \tag{26}$$

is solved in the fluid model, with $T_a = 500\,\mathrm{K}$, fixed atom flow velocity at the anode $V_a(0) = 142\,\mathrm{m/s}$ (Dirichlet condition), and the same recombination boundary condition given by Eq. (17). This allowed to recover qualitatively the atom flow velocity behavior, Fig. 21(b), but at the same time, the fluid model resulted in a completely stationary solution [Fig. 21(a)].

To better identify the role of the atom distribution in the hybrid model, we configured the shifted Maxwellian distributions[48] for atoms with various temperatures denoted as $T_{a,s}$ and the fixed shift velocity 150 m/s. Thus, the value of $T_{a,s} = 0\,\mathrm{K}$ corresponds to Case 2. It is that even a low spread for atom velocities, corresponding to $T_{a,s} \approx 50\,\mathrm{K}$, heavily damps the oscillation amplitude to the order 1 A, similar to what we obtained with the half-Maxwellian and $T_a = 500\,\mathrm{K}$.

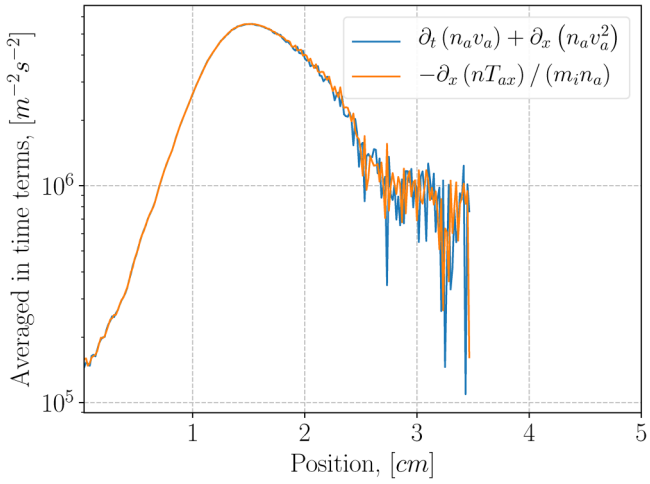

FIG. 20. Atom momentum balance equation terms evaluated from the hybrid model results. Note that the number of macroparticles (and atom density) significantly decrease to the right along the channel elevating the noise.

IV. CONCLUDING REMARKS AND SUMMARY

In this paper, low-frequency plasma dynamics in the axial direction of a Hall thruster are studied with full fluid and hybrid (kinetic/fluid) models. The model parameters are taken accordingly to the LANDMARK benchmarking fluid-hybrid test case.[32] In summary, our goal was not necessarily to exactly match the experimental data conditions but to identify missing physics in the fluid model and reveal important physics of the breathing oscillations. Benchmarking of the fluid and hybrid models shows a very close agreement for averaged plasma parameter profiles. Both models reveal the existence of the two different regimes of the low-frequency oscillations in Hall thrusters. While qualitatively, the two regimes are identifiable in both models, there are some quantitative differences in the frequencies and the amplitude of the oscillations. These differences are attributed to the ion finite thermal (pressure) effects, which were not originally included in the fluid model. Account of the finite ion pressure improves the agreement. The finite temperature spread of the neutral atoms provides a strong stabilizing effect on the oscillations as seen in both hybrid and fluid simulations.

It is found that in Case 1 (regime with co-existence of low- and high-frequency modes), the finite value of ion pressure played a

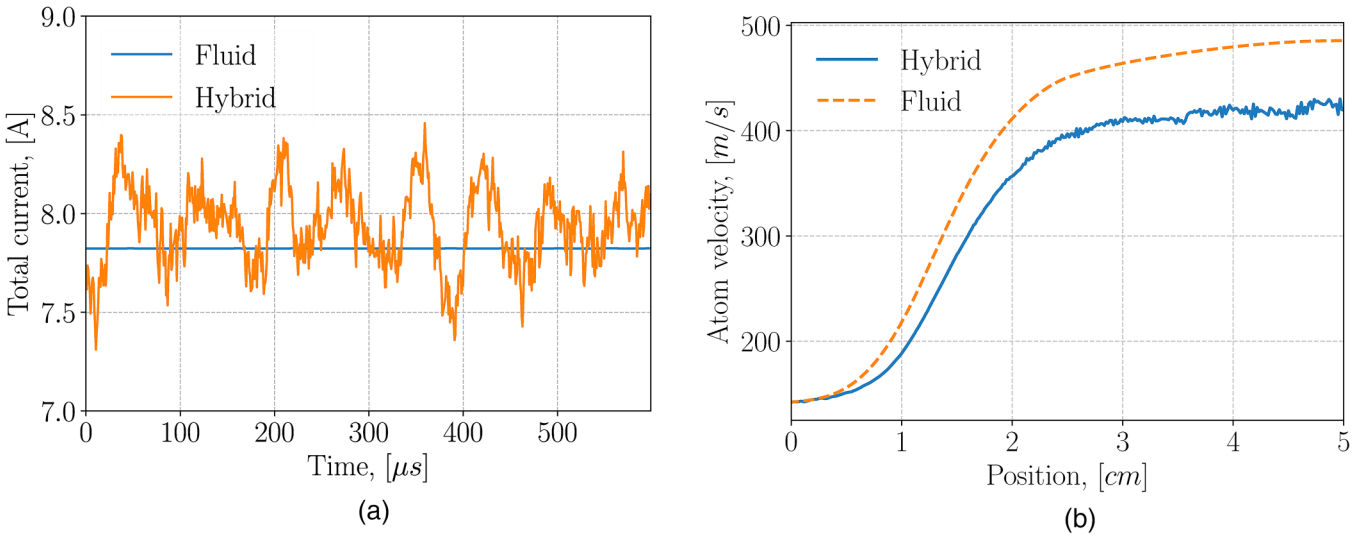

FIG. 21. The total current in fluid and hybrid simulations (a); comparison of a time-averaged spatial profile of an atom flow velocity for both models (b).

notable role in oscillatory behavior. Ion temperature is often assumed negligible in Hall thruster operation, similar to a neutral temperature, up to about 1000 K or 0.1 eV; thus, it was not included in the primary fluid model. Using a kinetic representation from the hybrid model, we show that the ion momentum balance without the ion pressure was notably violated. Thus, the ion pressure term with constant temperature was added into the fluid model. It resulted in a better conformity between the two models. Nevertheless, both fluid and hybrid models predicted the existence of two modes in this configuration even without the ion pressure in the fluid model, suggesting that these oscillations are the so-called resistive modes.[15,35] We believe that these modes are observed in the models without electron pressure, many of which were done in the primary studies and modeling of the axial dynamics of Hall thrusters.[1,15] We conjecture that the resistive modes of high frequencies play an important role in the excitation of the low-frequency modes.

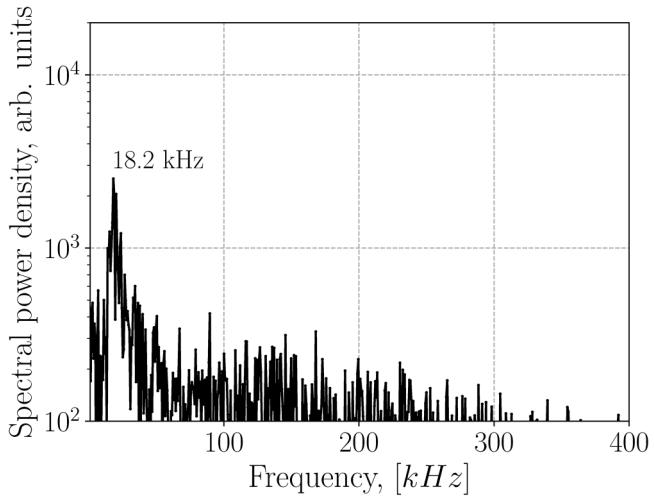

FIG. 22. Power spectrum of the total current in the hybrid simulation. Note that there is an increase in frequency (from 10.2 to 18.2 kHz) in comparison with Case 2 (with monokinetic atoms).

For Case 2, which shows only the low-frequency oscillations, we already performed extensive studies, Ref. 13, where we identified that the mechanism of these oscillations lies in the ion backflow region (presheath) and that they can be additionally reinforced with the plasma recombination. This led to the observation that the difference in the ion boundary conditions at the anode played a crucial role in our benchmark. The Bohm velocity for ions in the fluid model generated a larger atom yield due to the recombination from the anode, Eq. (17), in comparison with the hybrid model where this velocity was unconstrained and found to be smaller on average (thus leading to smaller atom yield). Replacing the Bohm condition with a free boundary condition in the fluid model resulted in better conformity between the two models. Similar to the previous case, we conclude that the main physical behavior was identified in both models even without this modification.

Finally, in Case 3, with a finite atom temperature in the hybrid model but the same values of other parameters as in Case 2, it is shown that the advection equation in the fluid model, Eq. (1), with the constant flow velocity is not sufficient to describe atom dynamics. An effect of selective ionization of neutral particles is observed in this case, where an average macroscopic velocity increased more than twice along the channel. The fluid model extended with the atom momentum balance equation (25) with a constant temperature resulted in a better agreement between the two models, reproducing the selective ionization effect and predicting a stationary solution. The hybrid model preserved the breathing oscillations (with a

similar frequency to Case 2) but with a much smaller amplitude. We were not able to find higher amplitude low-frequency oscillations for this case in the hybrid model (scanning parameters ν_ε or β_a). However, a small variation in the position of the maximum magnetic of the field profile (shifting it inside the channel), higher amplitude breathing modes were observed with thermal atoms. This important behavior needs further attention and is left for future studies.

The magnitude and profile of the anomalous mobility have a strong effect on the characteristics of the breathing mode. For the purposes of the comparison of the fluid and hybrid models, we used the empirical values of the anomalous collision frequency, which were often used in previous works[14,18,22,32] so that the anomalous mobility follows the magnetic field profile according to Eqs. (10)–(14). Our simulations reveal strong sensitivity of the breathing oscillations on the location of the magnetic field maximum. Anomalous electron mobility and diffusion remain the critical parameters that are poorly known in theory and experiments. Further work on calibrating the models against experimental data is required.[22,52]

ACKNOWLEDGMENTS

This work was supported in part by NSERC Canada and the U.S. Air Force Office of Scientific Research (No. FA9550-15-1-0226), NSERC Canada, and Compute Canada for providing the computational resources.

AUTHOR DECLARATIONS

Conflict of Interest

The authors have no conflicts to disclose.

Author Contributions

O. Chapurin: Conceptualization (lead); Data curation (lead); Formal analysis (lead); Investigation (lead); Methodology (equal); Project administration (equal); Software (lead); Validation (equal); Visualization (lead); Writing – original draft (lead); Writing – review and editing (lead). **A. I. Smolyakov:** Conceptualization (equal); Funding acquisition (lead); Investigation (equal); Methodology (equal); Project administration (lead); Resources (equal); Supervision (lead); Validation (equal); Writing – original draft (supporting); Writing – review and editing (equal). **G. Hagelaar:** Conceptualization (equal); Investigation (equal); Methodology (equal); Project administration (supporting); Resources (equal); Software (equal); Supervision (equal); Validation (equal); Writing – original draft (supporting); Writing – review and editing (supporting). **J.-P. Boeuf:** Conceptualization (supporting); Investigation (supporting); Methodology (supporting); Project administration (supporting); Resources (equal); Validation (equal); Writing – original draft (supporting); Writing – review and editing (supporting). **Y. Raitses:** Conceptualization (supporting); Methodology (supporting); Validation (equal); Writing – original draft (supporting); Writing – review and editing (supporting).

DATA AVAILABILITY

The data that support the findings of this study are available from the corresponding author upon reasonable request.

APPENDIX A: RESISTIVE MODES

Here, we present the cases with more prominent resistive modes and show their effect on the ion heating, which is the extension to Case 1. It is found that the larger value of the anomalous (electron) energy loss frequency, $\nu_{\varepsilon,\mathrm{in}} = 1.2 \times 10^7\ \mathrm{s}^{-1}$, leads to the solution where the resistive mode dominates; see Fig. 23(a). It reveals a larger amplitude and clearly distinct high-frequency oscillations (168 kHz), with a small low-frequency modulation

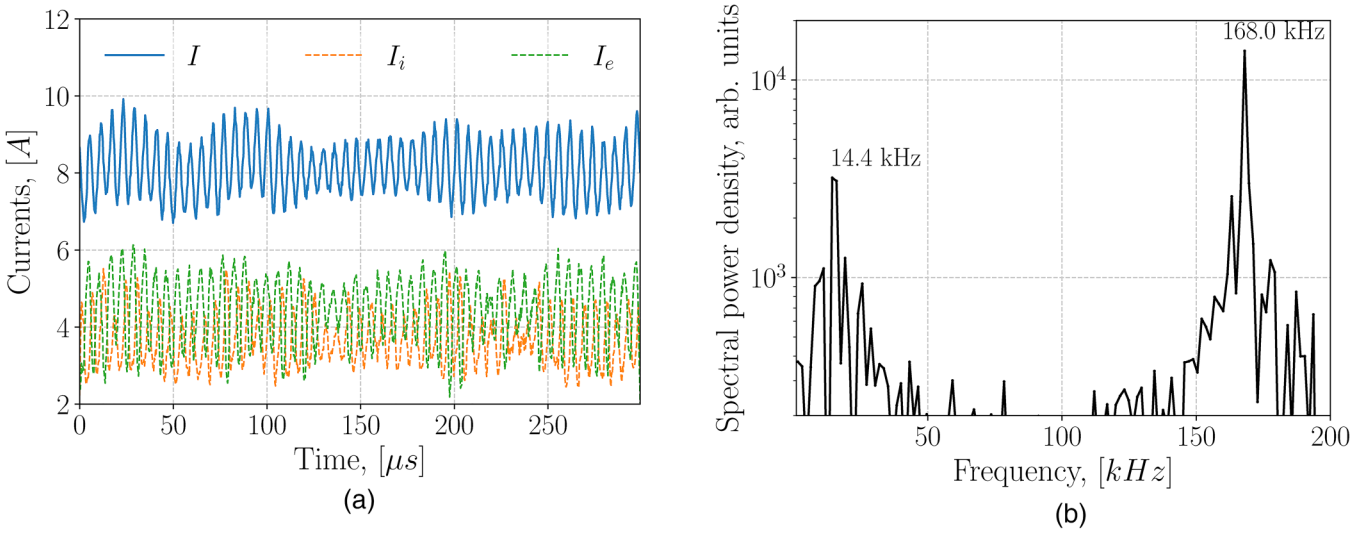

FIG. 23. Currents (a) and the total current spectra (b).

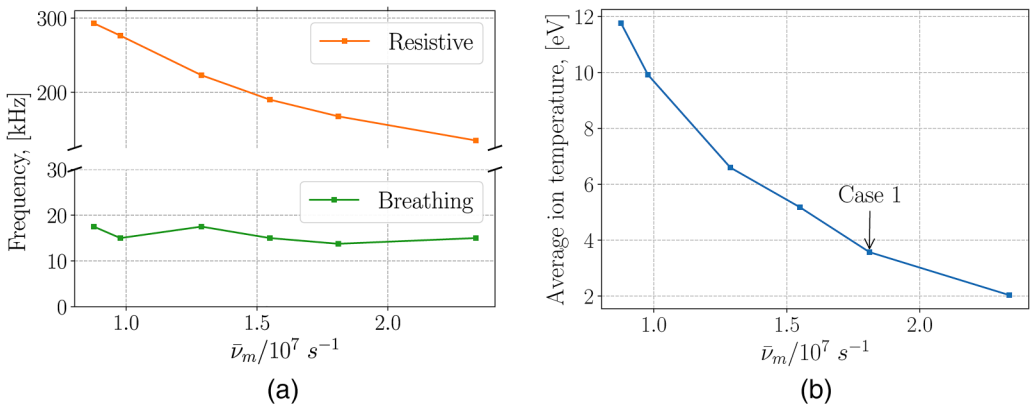

FIG. 25. Frequency of breathing and resistive modes as a function of averaged (over time and space inside the channel) total electron momentum exchange frequency $\bar{\nu}_m$ (a). Average ion temperature (in time and whole domain) as a function of $\bar{\nu}_m$ (b). The parameter varied in this study was the anomalous Bohm coefficient $\beta_{a,in}$ inside the channel, directly affecting the total electron frequency, Eq. (11).

(14.4 kHz); Fig. 23(b) shows its spectrum. As it was demonstrated for Case 1, ion temperature effects were not negligible, and ions were heated to a few electron volts. We noticed that the average ion temperature is higher with the presence of the resistive modes as shown in Fig. 24, where the resistive modes appear for values $\nu_{\varepsilon,\text{in}} = 0.9\,\text{s}^{-1}$ and higher.

Now, we show that the frequency of the resistive mode scales with the average electron collision frequency $\bar{\nu}_m$, Fig. 25(a), and thus, the higher electron mobility $\approx 1/\bar{\nu}_m$ leads to higher frequencies. At the same time, the ion heating effect is stronger for the higher frequency of resistive modes, Fig. 25(b). It is interesting to note that the breathing mode frequency stays approximately the same, Fig. 25(a), along with the size of the presheath region.

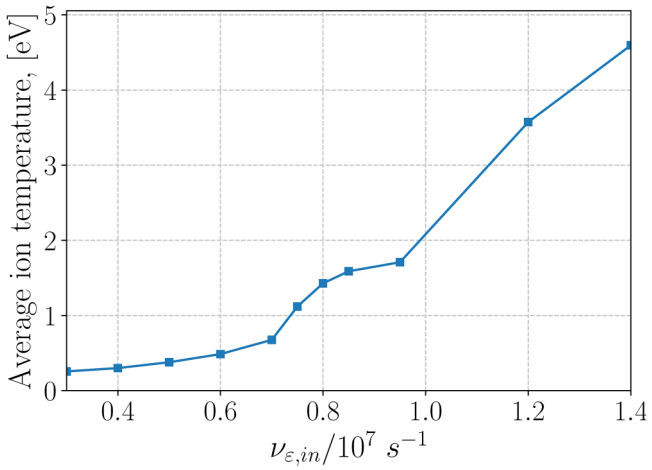

FIG. 24. Ion average thermal energy as a function of the anomalous electron energy loss coefficient. As we move into the regime with resistive modes present (studied in Case 1), ion heating increases and ion pressure effects may become important.

APPENDIX B: IONIZATION RATE AND ENERGY LOSS FUNCTIONS

The ionization rate $\beta(\varepsilon) = \langle\sigma(v)v\rangle$ as a function of electron energy ε is obtained by averaging over Maxwellian EEDF with the cross sections from the SIGLO database.[53] The collisional energy loss coefficient K(ε) is generated by BOLSIG+[54] as a table-valued function. Both functions are shown in Fig. 26.

APPENDIX C: NUMERICAL METHODS FOR A FLUID MODEL

The time-dependent fluid model, given by Eqs. (1), (2), (3), and (6), is solved via the BOUT++[29] computational framework. The CVODE solver from the SUNDIALS package[55] was used to solve the algebraic-differential system resulting from the method of

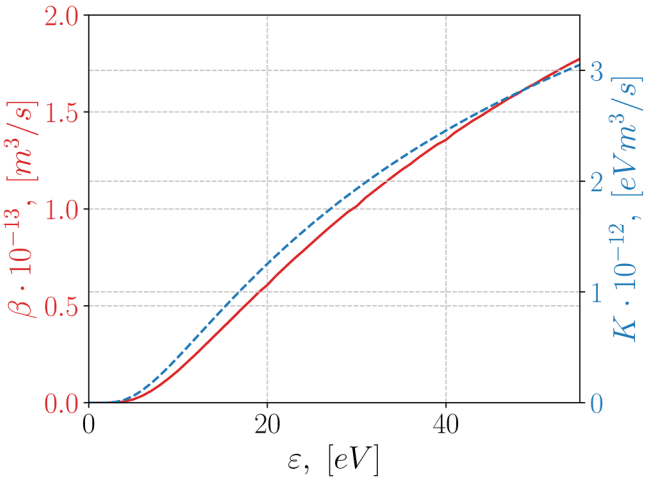

FIG. 26. Ionization rate β and electron ionization energy loss coefficient K.

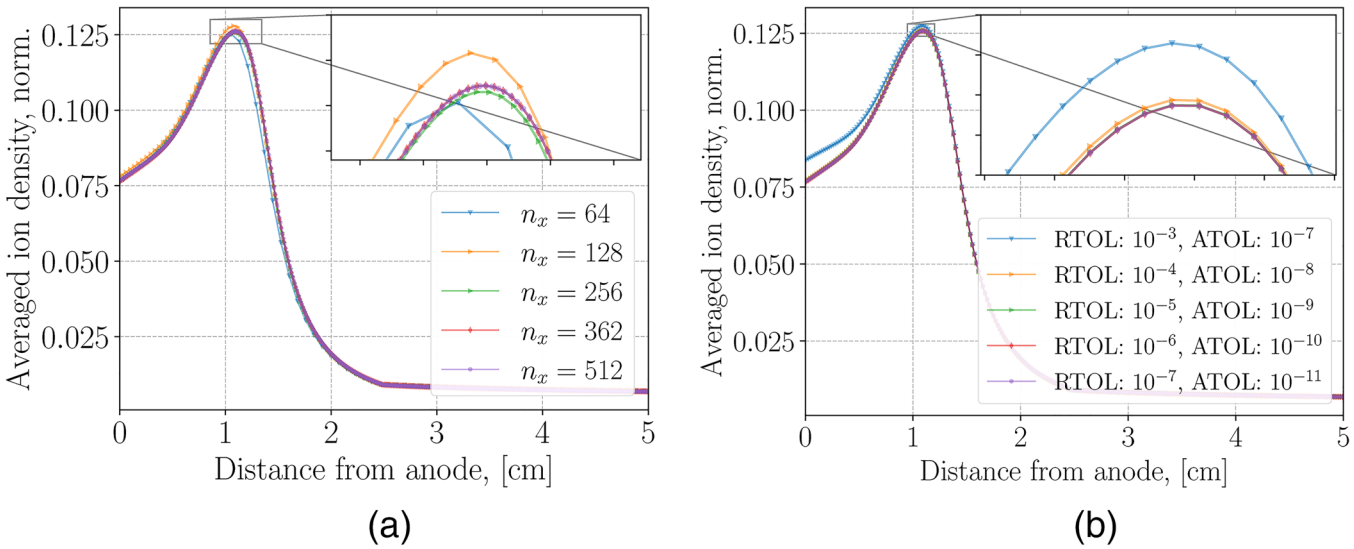

FIG. 27. Ion density spatial profile, averaged over ten time periods of its main low-frequency mode, where the parameters correspond to Case 2. Convergence with grid size (a) with the fixed ODE solver tolerances: relative is 10^{-5} and absolute is 10^{-9}. Convergence with the CVODE tolerances (b) with the fixed number of grid points: $n_x = 256$.

lines utilized in BOUT++. The upwind terms are discretized with the WENO 3rd order scheme and other terms with the 2nd order central-difference scheme. Figures 27(a) and 27(b) demonstrate the convergence of solutions of Case 2 with the various grid sizes and various ODE integrator tolerances. Based on these results, the number of grid points is set to $n_x = 256$, and the relative and absolute tolerances for the CVODE are set to 10^{-5} and 10^{-8}, respectively. The fluid equations are normalized, and the normalization scheme is the following. The system length L_0 and a typical ion-sound velocity $c_s = \sqrt{T_e/m_i}$, where $T_e = 20\,\text{eV}$, are chosen as the basis for normalization, and they form the characteristic frequency $f_0 = c_s/L_0$. Densities are normalized to the neutral density at the anode $N_0 = n_a(0, t) = \dot{m}/m_i A V_a$. The normalization scheme is

$$t^* = f_0 t,\ x^* = \frac{x}{L_0},\ E^* = E\frac{eL_0}{m_i V_0^2},\ j^* = \frac{j}{eN_0 V_0},\ \mu_e^* = \mu_e \frac{m_i f_0}{e},\ \beta^* = \frac{\beta N_0}{f_0}.$$

REFERENCES

[1]A. I. Morozov and V. V. Savelyev, "Fundamentals of stationary plasma thruster theory," in *Reviews of Plasma Physics* (Springer, 2000), pp. 203–391.

[2]A. I. Smolyakov, O. Chapurin, W. Frias, O. Koshkarov, I. Romadanov, T. Tang, M. Umansky, Y. Raitses, I. D. Kaganovich, and V. P. Lakhin, "Fluid theory and simulations of instabilities, turbulent transport and coherent structures in partially-magnetized plasmas of discharges," Plasma Phys. Control. Fusion **59**(1), 014041 (2017).

[3]T. Lafleur, S. D. Baalrud, and P. Chabert, "Theory for the anomalous electron transport in Hall effect thrusters. I. Insights from particle-in-cell simulations," Phys. Plasmas **23**(5), 053502 (2016).

[4]S. Janhunen, A. Smolyakov, O. Chapurin, D. Sydorenko, I. Kaganovich, and Y. Raitses, "Nonlinear structures and anomalous transport in partially magnetized E × B plasmas," Phys. Plasmas **25**(1), 011608 (2018).

[5]S. Janhunen, A. Smolyakov, D. Sydorenko, M. Jimenez, I. Kaganovich, and Y. Raitses, "Evolution of the electron cyclotron drift instability in two-dimensions," Phys. Plasmas **25**(8), 082308 (2018).

[6]W. Villafana, F. Petronio, A. C. Denig, M. J. Jimenez, D. Eremin, L. Garrigues, F. Taccogna, A. Alvarez-Laguna, J.-P. Boeuf, A. Bourdon, P. Chabert, T. Charoy, B. Cuenot, K. Hara, F. Pechereau, A. Smolyakov, D. Sydorenko, A. Tavant, and O. Vermorel, "2D radial-azimuthal particle-in-cell benchmark for E × B discharges," Plasma Sources Sci. Technol. **30**(7), 075002 (2021).

[7]M. Jimenez, "2D3V particle-in-cell simulations of electron cyclotron drift instability and anomalous electron transport in E × B plasmas," Master's thesis (University of Saskatchewan, 2021).

[8]I. D. Kaganovich, A. Smolyakov, Y. Raitses, E. Ahedo, I. G. Mikellides, B. Jorns, F. Taccogna, R. Gueroult, S. Tsikata, A. Bourdon, J.-P. Boeuf, M. Keidar, A. T. Powis, M. Merino, M. Cappelli, K. Hara, J. A. Carlsson, N. J. Fisch, P. Chabert, I. Schweigert, T. Lafleur, K. Matyash, A. V. Khrabrov, R. W. Boswell, and A. Fruchtman, "Physics of E × B discharges relevant to plasma propulsion and similar technologies," Phys. Plasmas **27**(12), 120601 (2020).

[9]Y. B. Esipchuk, A. I. Morozov, G. N. Tilinin, and A. V. Trofimov, "Plasma oscillations in closed-drift accelerators with an extended acceleration zone," Sov. Phys. Tech. Phys. **18**, 928 (1974).

[10]J. Fife, M. Martinez-Sanchez, J. Szabo, J. Fife, M. Martinez-Sanchez, and J. Szabo, "A numerical study of low-frequency discharge oscillations in Hall thrusters," in *33rd Joint Propulsion Conference and Exhibit* (American Institute of Aeronautics and Astronautics, 2012), p. 3052.

[11]S. Barral and E. Ahedo, "On the origin of low frequency oscillations in Hall thrusters," AIP Conf. Proc. **993**(1), 439–442 (2008).

[12]K. Hara, M. J. Sekerak, I. D. Boyd, and A. D. Gallimore, "Perturbation analysis of ionization oscillations in Hall effect thrusters," Phys. Plasmas **21**(12), 122103 (2014).

[13]O. Chapurin, A. I. Smolyakov, G. Hagelaar, and Y. Raitses, "On the mechanism of ionization oscillations in Hall thrusters," J. Appl. Phys. **129**(23), 233307 (2021).

[14]T. Lafleur, P. Chabert, and A. Bourdon, "The origin of the breathing mode in Hall thrusters and its stabilization," J. Appl. Phys. **130**(5), 053305 (2021).

[15]S. Chable and F. Rogier, "Numerical investigation and modeling of stationary plasma thruster low frequency oscillations," Phys. Plasmas **12**(3), 033504 (2005).
[16]L. Q. Wei, L. Han, D. R. Yu, and N. Guo, "Low-frequency oscillations in Hall thrusters," Chin. Phys. B **24**(5), 055201 (2015).
[17]K. Makowski, Z. Peradzynski, S. Barral, and M. A. Dudeck, "Review of the plasma fluid models in stationary plasma thrusters," High Temp. Mater. Process. **5**(2), 13 (2001).
[18]G. J. M. Hagelaar, J. Bareilles, L. Garrigues, and J.-P. Boeuf, "Modelling of stationary plasma thrusters," Contrib. Plasma Phys. **44**(56), 529–535 (2004).
[19]J.-P. Boeuf and L. Garrigues, "Low frequency oscillations in a stationary plasma thruster," J. Appl. Phys. **84**(7), 3541–3554 (1998).
[20]S. Barral, Z. Peradzynski, K. Makowski, and M. A. Dudeck, "Fluid model of Hall thruster—Comparison with hybrid model," High Temp. Mater. Process. **5**(2), 11 (2001).
[21]S. Barral and E. Ahedo, "Low-frequency model of breathing oscillations in Hall discharges," Phys. Rev. E **79**(4), 046401 (2009).
[22]V. Giannetti, M. M. Saravia, L. Leporini, S. Camarri, and T. Andreussi, "Numerical and experimental investigation of longitudinal oscillations in Hall thrusters," Aerospace **8**(6), 148 (2021).
[23]D. Yu, C. Wang, L. Wei, C. Gao, and G. Yu, "Stabilizing of low frequency oscillation in Hall thrusters," Phys. Plasmas **15**(11), 113503 (2008).
[24]S. Barral and J. Miedzik, "Numerical investigation of closed-loop control for Hall accelerators," J. Appl. Phys. **109**(1), 013302 (2011).
[25]L. Wei, K. Han, C. Wang, H. Li, C. Zhang, and D. Yu, "Study on breathing mode oscillation suppression of self-excited Hall thrusters," J. Vac. Sci. Technol. A **30**(6), 061304 (2012).
[26]A. I. Morozov and V. V. Savel'ev, "One-dimensional hybrid model of a stationary plasma thruster," Plasma Phys. Rep. **26**(10), 875–880 (2000).
[27]A. Shashkov, A. Lovtsov, and D. Tomilin, "A one-dimensional with three-dimensional velocity space hybrid-PIC model of the discharge plasma in a Hall thruster," Phys. Plasmas **24**(4), 043501 (2017).
[28]M. B. Gavrikov and A. A. Taiurskii, "Hybrid model of a stationary plasma thruster," J. Phys.: Conf. Ser. **2028**, 012002 (2021) (in Russian).
[29]B. D. Dudson, M. V. Umansky, X. Q. Xu, P. B. Snyder, and H. R. Wilson, "BOUT++: A framework for parallel plasma fluid simulations," Comput. Phys. Commun. **180**(9), 1467–1480 (2009).
[30]G. J. M. Hagelaar, J. Bareilles, L. B. J. P. Garrigues, and J.-P. Boeuf, "Two-dimensional model of a stationary plasma thruster," J. Appl. Phys. **91**(9), 5592–5598 (2002).
[31]G. J. M. Hagelaar, J. Bareilles, L. Garrigues, and J.-P. Boeuf, "Role of anomalous electron transport in a stationary plasma thruster simulation," J. Appl. Phys. **93**(1), 67–75 (2003).
[32]See https://www.landmark-plasma.com/ for "Low temperAture magNetizeD plasMA benchmaRKs."
[33]A. A. Litvak and N. J. Fisch, "Resistive instabilities in Hall current plasma discharge," Phys. Plasmas **8**(2), 648–651 (2001).
[34]E. Fernandez, M. K. Scharfe, C. A. Thomas, N. Gascon, and M. A. Cappelli, "Growth of resistive instabilities in E × B plasma discharge simulations," Phys. Plasmas **15**(1), 012102 (2008).
[35]O. Koshkarov, A. I. Smolyakov, I. V. Romadanov, O. Chapurin, M. V. Umansky, Y. Raitses, and I. D. Kaganovich, "Current flow instability and nonlinear structures in dissipative two-fluid plasmas," Phys. Plasmas **25**(1), 011604 (2018).
[36]A. I. Morozov and V. V. Savelýev, "One-dimensional hydrodynamic model of the atom and ion dynamics in a stationary plasma thruster," Plasma Phys. Rep. **26**(3), 219–224 (2000).
[37]M. B. Gavrikov and A. A. Taiurskii, "Some mathematical questions of plasma ionization," Prepr. Keldysh Inst. Appl. Math. **94**, 1–48 (2021) (in Russian).
[38]G. Hagelaar and S. Sadouni, "Instabilities in fluid simulations of E × B plasmas," Bull. Am. Phys. Soc. **59**, 014041 (2017).
[39]S. Sadouni, G. Hagelaar, and A. Smolyakov, "Fluid modeling and linear analysis of instabilities in E × B discharge plasmas in Hall thrusters," in *APS Annual Gaseous Electronics Meeting Abstracts* (APS Meeting Abstracts, 2018), p. LW1-013.
[40]S. Sadouni, "Fluid modeling of transport and instabilities in magnetized low-temperature plasma sources," Ph.D. thesis (Université Paul Sabatier-Toulouse III, 2020).
[41]A. Cohen-Zur, A. Fruchtman, J. Ashkenazy, and A. Gany, "Analysis of the steady-state axial flow in the Hall thruster," Phys. Plasmas **9**(10), 4363–4374 (2002).
[42]E. Ahedo and J. Rus, "Vanishing of the negative anode sheath in a Hall thruster," J. Appl. Phys. **98**(4), 043306 (2005).
[43]L. Dorf, V. Semenov, and Y. Raitses, "Anode sheath in Hall thrusters," Appl. Phys. Lett. **83**(13), 2551–2553 (2003).
[44]L. Dorf, Y. Raitses, and N. J. Fisch, "Experimental studies of anode sheath phenomena in a Hall thruster discharge," J. Appl. Phys. **97**(10), 103309 (2005).
[45]G. Hagelaar, "Modelling methods for low-temperature plasmas," Habilitation thesis (Université Paul Sabatier, 2008).
[46]A. Smolyakov, O. Chapurin, I. Romadanov, Y. Raitses, I. Kaganovich, G. Hagelaar, and J.-P. Boeuf, "Stationary profiles and axial mode oscillations in Hall thrusters," in *AIAA Propulsion and Energy 2019 Forum* (AIAA, 2019), p. 4080.
[47]C. K. Birdsall, "Particle-in-cell charged-particle simulations, plus Monte Carlo collisions with neutral atoms, PIC-MCC," IEEE Trans. Plasma Sci. **19**(2), 65–85 (1991).
[48]K. L. Cartwright, J. P. Verboncoeur, and C. K. Birdsall, "Loading and injection of Maxwellian distributions in particle simulations," J. Comput. Phys. **162**(2), 483–513 (2000).
[49]N. B. Meezan, W. A. Hargus, Jr., and M. A. Cappelli, "Anomalous electron mobility in a coaxial Hall discharge plasma," Phys. Rev. E **63**(2), 026410 (2001).
[50]W. A. Hargus and M. A. Cappelli, "Interior and exterior laser-induced fluorescence and plasma measurements within a Hall thruster," J. Propul. Power **18**(1), 159–168 (2002).
[51]K. Hara, I. D. Boyd, and V. I. Kolobov, "One-dimensional hybrid-direct kinetic simulation of the discharge plasma in a Hall thruster," Phys. Plasmas **19**(11), 113508 (2012).
[52]B. Jorns, "Predictive, data-driven model for the anomalous electron collision frequency in a Hall effect thruster," Plasma Sources Sci. Technol. **27**(10), 104007 (2018).
[53]SIGLO database; see www.lxcat.net/SIGLO; accessed June 2013.
[54]G. J. M. Hagelaar and L. C. Pitchford, "Solving the Boltzmann equation to obtain electron transport coefficients and rate coefficients for fluid models," Plasma Sources Sci. Technol. **14**(4), 722 (2005).
[55]A. C. Hindmarsh, P. N. Brown, K. E. Grant, S. L. Lee, R. Serban, D. E. Shumaker, and C. S. Woodward, "SUNDIALS: Suite of nonlinear and differential/algebraic equation solvers," ACM Trans. Math. Softw. **31**(3), 363–396 (2005).